

THESIS FOR THE DEGREE OF LICENTIATE OF ENGINEERING

**Microstructural evolution during hot  
compression of a Ni-base superalloy:  
Dynamic and post-dynamic recrystallization below the  
secondary carbide solvus temperature**

Emil Eriksson



Department of Physics

CHALMERS UNIVERSITY OF TECHNOLOGY

Göteborg, Sweden 2021

Microstructural evolution during hot compression of a Ni-base superalloy: Dynamic and post-dynamic recrystallization below the secondary carbide solvus temperature  
Emil Eriksson

© Emil Eriksson, 2021.

Department of Physics  
Chalmers University of Technology  
SE-412 96 Göteborg  
Sweden  
Telephone + 46 (0)31-772 1000

Cover illustration

The figure illustrates inverse pole figure maps acquired with electron backscattered diffraction. The left figure shows a microstructure after dynamic recrystallization while the figure on the right a post-dynamic recrystallized one.

Printed by Chalmers Reproservice  
Göteborg, Sweden 2021

Microstructural evolution during hot compression of a Ni-base superalloy: Dynamic and post-dynamic recrystallization below the secondary carbide solvus temperature

Emil Eriksson

Department of Physics

Chalmers University of Technology

## Abstract

With an increased demand to lower emissions, the efficiency of aircraft engines have to be improved. One way to achieve this is to increase the operation temperature. However, due to the extremely challenging environments in the hot sections of these engines, the current alloys are at their limits.

Today, Ni-base superalloys are the materials used for these sections, given their outstanding ability to maintain their strength at temperatures up to 0.8 of their melting temperature, as well as showing excellent corrosion and oxidation resistances. New Ni-base superalloys are developed for these challenges and one of them, Haynes 282, is the alloy investigated in this thesis. In order to tailor an alloys mechanical properties to best suit the needs, the microstructure has be to be processed. The initial working steps for wrought superalloys is forging, which sets the base of the microstructure of all subsequent processing steps. An understanding of how the forging parameters will affect the microstructure is therefore crucial.

The dynamic recrystallization mechanisms of the Ni-base superalloy Haynes 282 during hot deformation in a Gleeble were first investigated. Temperatures both below and above the carbide solvus temperature were studied in order to determine how these parameters affect the resulting microstructure. The microstructures were investigated using electron backscattered diffraction and electron channelling contrast imaging in scanning electron microscopes. In order to simulate industrial conditions, samples were held at temperature after deformation in order to evaluate the post dynamic recrystallization phenomena occurring in the Ni-base superalloy for each temperature and strain rate investigated. The microstructures from samples with and without post-deformation hold were compared. An investigation regarding the role of secondary carbides present at grain boundaries during deformation below carbide solvus was also performed, showing that secondary carbides do not affect the recrystallization significantly. Parameters like temperature and strain rate have a larger impact.

**Keywords:** Ni-base superalloys, Hot compression, Recrystallization, Electron microscopy



# Preface

The research work presented in this thesis was carried out at the Division of Materials Microstructure at the Department of Physics, Chalmers University of Technology, during the time period March 2018 - March 2021, under the supervision of Associate Professor Magnus Hörnqvist Colliander, Researcher Mohammad Sattari and Associate Professor Joel Andersson (University West, Trollhättan, Sweden).

This research is funded by the the Swedish Agency for Innovation (VINNOVA), through the Swedish National Aeronautical Research Program (NFFP) grant no. 2017-04863, in collaboration with GKN Aerospace Engine Systems AB. The material was supplied by GKN Aerospace Engine Systems, Trollhättan, Sweden.

## List of appended papers

- I. *Dynamic and post dynamic recrystallization of Haynes 282 below the secondary carbide solvus*  
E. Eriksson, M. Hörnqvist Colliander  
Submitted to Metals.
- II. *The effect of grain boundary carbides during hot compression of Ni-based superalloy Haynes 282*  
E. Eriksson, M. Hörnqvist Colliander  
In Manuscript.

## My contributions to the appended papers

- I. I was a part of deciding the sample matrix, did the hot compression experiments with the assistance of Kjell Hurtig (University West) and Fabian Hanning (University West), EBSD analysis , analysed and evaluated the data, wrote the first draft and edited the paper.
- II. I was a part of deciding the sample matrix, did the hot compression experiments with the assistance of Kjell Hurtig (University West) and Fabian Hanning (University West), EBSD analysis, analysed and evaluated the data, wrote the first draft and edited the paper.

# Acknowledgements

My deepest gratitude goes out to my supervisor Dr. Magnus Hörnqvist Colliander for his tremendous support. I am grateful that you chose me as the student for this project, for the time you take and the patience you show during our discussions. Your supervision and guidance helps me to better tackle my results from logical, thorough and academic perspectives. I thank GKN Aerospace AB, and Ceena Joseph as project supervisor especially. Your support and knowledge on superalloys has helped me a lot with my work. I also thank Yiming Yao and Adrianna Lozinko at the department of Industrial and Materials Science for their help with sample polishing and handling the muffle furnace, Kjell Hurtig and Fabian Hanning at University West for their many hours of support with the Gleeble experiments and of course the staff at the Chalmers Material Analysis Laboratory who taught me to operate all electron microscopes I have used. A special thanks to Ola Löfgren for his quick help in regards to computer issues.

I am also grateful for all my colleagues at my division, Eva Olsson Group and the CMAL staff who were there for discussions, and coffee breaks and that you created a friendly work environment that was encouraging during the more stressful times most PhD students experience at one point or another. A special thanks to Anand who taught me how to perform EBSD analysis, and Kristina who taught me the ropes when I started.

I am grateful for my mother and late father who always supported my decisions in life and who continue to do so to their best extent. You of course hold the main responsibility in what kind of person I turned out to be, and I think (and hope) many agree that you did a good job of it.

I also extend a thank you to my personal trainer Annica Ingemann, who has helped me maintain a healthy body, after hours of sitting at a desk, and letting out my frustrations by lifting weights until no energy is left to think about them.



---

# Contents

---

<b>1</b>	<b>Introduction</b>	<b>1</b>
1.1	Background . . . . .	1
1.2	Motivation . . . . .	2
1.3	Aim of the study . . . . .	3
<b>2</b>	<b>Ni-base superalloys</b>	<b>5</b>
2.1	Superalloys in general . . . . .	5
2.2	Phases in Ni-base superalloys . . . . .	5
2.2.1	The $\gamma$ phase . . . . .	5
2.2.2	Intragranular precipitates . . . . .	6
2.2.3	Intergranular precipitates . . . . .	7
2.3	Haynes 282 . . . . .	8
2.4	Hot working . . . . .	10
<b>3</b>	<b>Recrystallization</b>	<b>13</b>
3.1	Dynamic recrystallization and mechanical response . . . . .	14
3.2	Dynamic recrystallization in Ni-base superalloys . . . . .	18
<b>4</b>	<b>Experimental Methods</b>	<b>21</b>
4.1	Thermomechanical deformation . . . . .	21
4.1.1	Sample preparation . . . . .	21

4.1.2	Gleeble . . . . .	21
4.2	Microstructural characterization . . . . .	24
4.2.1	Sample preparation . . . . .	24
4.2.2	Scanning electron microscopy . . . . .	25
<b>5</b>	<b>Results and discussion</b>	<b>31</b>
5.1	Initial structure . . . . .	32
5.2	Dynamic recrystallization at sub-solvus temperatures . . . . .	32
5.2.1	Mechanical response . . . . .	32
5.2.2	Recrystallization . . . . .	35
5.3	Effect of secondary grain boundary carbides . . . . .	40
5.4	Effect of post dynamic recrystallization . . . . .	46
<b>6</b>	<b>Future research</b>	<b>51</b>
	<b>Bibliography</b>	<b>53</b>

# CHAPTER 1

---

## Introduction

---

### 1.1 Background

With an increasing understanding of the consequences caused by pollution, sectors like the aero engine and gas turbine industries are striving to increase the efficiency of the combustion process in order to reduce fuel consumption and pollution levels. This is today the main factor driving the development for aero industry who are dedicating research to develop materials that can better withstand the harsh environments occurring in the hot sections of jet engines. Combustion at higher temperatures increases the efficiency [1], and thereby decreases the pollution levels.

Inside the hot sections of aero engines and gas turbine generators, the environment is corrosive with high temperatures and mechanical loads. Aero engines are also safety-critical applications where severe consequences of failure makes the choice of material crucial.

In the early history of gas turbines, different kinds of steels were employed as these were the only materials that could withstand the temperatures. However, as temperatures in the hot sections increased, no steel available was able to meet the requirements. New types of alloys were developed. These were

named superalloys due to their excellent high temperature strength and corrosion resistance. Three categories of superalloys were developed, based on the base metal they consisted of: Fe, Ni and Co-superalloys. Out of these, the Ni-base superalloys are the best suited, and most widely used, for the hottest sections of engines and turbines due to their excellent creep and failure properties as well as ability to withstand load at temperatures up to 0.8 of their melting temperature [2]. Today, numerous types of superalloys exist, with different strengthening phases. Components are used both as single crystals and polycrystalline. However, with increasing demands on efficiency and manufacturing, new superalloys have to be developed and optimal combinations of fabricability and service stability have to be found. Due to their complex chemistry, often with 10 or more alloying elements, small changes to the ratios can alter the microstructure and therefore, the properties. Transmitting results from one alloy to another is not necessarily viable.

## 1.2 Motivation

Ni-base superalloys are well adapted to operate at high service temperatures and corrosive environments that exist in the hot sections of aero engines and gas turbine generators. They receive these properties from multiple strengthening phases, dependent on alloying content, that are either intra- or intergranular.

Haynes 282, developed by Haynes International, is a relatively new competitor to existing  $\gamma/\gamma'$  superalloys like Waspaloy and René 41. It has a slightly lower  $\gamma'$  fraction compared to these alloys, with its equilibrium fraction being around 20 % in a fully heat treated condition. The kinetics for  $\gamma'$  nucleation and growth are also slow compared to other alloys, which improves weldability and fabricability, [3].

Most previous research on the microstructure of Haynes 282 has been focused on the mechanical properties [4–9], heat treatments [10, 11] or microstructure stability and related effects [12, 13]. All of these studies have used material already in its forged condition. Parameters employed during initial hot working operations, such as forging, set the basis for the microstructure during subsequent processing, like heat treatments, and the mechanical properties obtained after all processing has been done. Understanding the effect of forging on the resulting microstructure is therefore very important, but it is relatively un-researched ground for this particular alloy. Some research has been done [14, 15] at a range of temperatures and strain rates. The research presented in the thesis aims to further develop the understanding of forging below the carbide solvus temperature from a more industrial point of view. In industry, components are air cooled leading to a continued changing of the microstructure

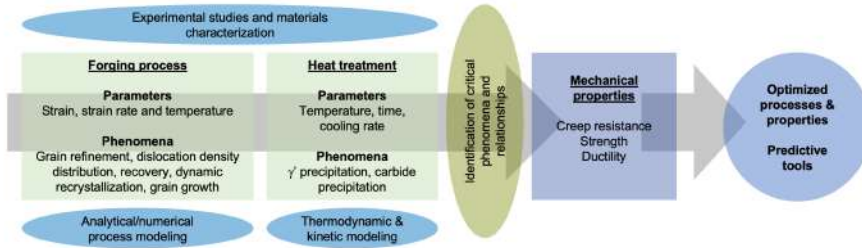


Figure 1.1: Project outline, with the three milestones: forging operations, heat treatments and mechanical properties.

after deformation. This was investigated by Gardner et al. [15] but above the carbide solvus temperature. Shi et al. [14] performed hot compression both above and below, but prior to compression, the samples were soaked above carbide solvus. Soaking refers to the time a component is held at the target temperature in order to stabilize the temperature before deformation starts. If this is done below the carbide solvus, secondary carbides would nucleate and grow at grain boundaries.

Improving the low cycle fatigue properties for certain pieces in the hot sections would improve the overall efficiency. A microstructure with smaller grains could achieve this improvement, and forging at lower temperatures could result in a proper grain size. This study aims to evaluate the microstructure from forging at lower temperatures, to in later studies correlate it to the mechanical properties.

The project can therefore be divided into three milestones, as shown in figure 1.1. The first milestone, forging process, is what this thesis covers. The next objective will be to continue the thermomechanical procedures employed for Ni-base superalloys, which are heat treatments. Here, the microstructure received from forging is further improved by introducing strengthening precipitates. Finally, the mechanical properties received after these operations will be evaluated.

### 1.3 Aim of the study

The aim is to understand the dynamic recrystallization phenomena occurring in the Ni-base superalloy Haynes 282 at temperatures below the secondary carbide solvus temperature, around 1100 °C, and understand the processes leading to the resulting microstructures after deformation at these temperatures. Specifically the research questions addressed in this thesis are:

- How does hot deformation below the carbide solvus temperature develop the microstructure?
- What is the role of carbides during this process?
- How does the microstructure develop during the high temperature hold periods after deformation?

# CHAPTER 2

---

## Ni-base superalloys

---

### 2.1 Superalloys in general

Ni-base superalloys are mainly used in the hot parts of aero engines or stationary turbine generators [1]. They have excellent mechanical stability at high temperatures and highly corrosive environments, which they receive from their complex structure. Common for all types of Ni-base superalloys are that they consist of a solution strengthened matrix  $\gamma$ . Some alloys are also strengthened with precipitated intra-, and intergranular secondary phases, depending on alloying elements.

### 2.2 Phases in Ni-base superalloys

#### 2.2.1 The $\gamma$ phase

The  $\gamma$  phase has a disordered face-centered cubic (fcc) crystal structure. It consists of Ni and elements with similar atomic radii (variations between 1-13%) as Ni, e.g. Co, Fe, Cr, Mo, W, Ti and Al [16]. One mechanism of solid solution strengthening is created by the difference in atomic radii. Because

the matrix is disordered, there are no fixed lattice sites for elements. Placing an atom of different size than Ni will create local elastic strains around the solute atom. The strengthening mechanism comes from this strain acting on dislocations, hindering their movement compared to an unstrained lattice of pure Ni atoms. Another factor contributing to the strengthening of alloying elements in the matrix is the lowering of the stacking fault energy,  $\gamma_{SFE}$ , which hinders cross slip of dislocations through the matrix [16] and the changing of  $\gamma_{SFE}$  has been correlated with the number of valency electrons for the solute elements [16]. The alloying elements can also offer other benefits than solid solution strengthening. Cr offers corrosion resistance [17], Al oxidation resistance while Mo and Co raises the solvus temperature for  $\gamma'$  particles [16, 18].

Which phases precipitate in a certain Ni-base superalloy varies based on alloying content. They can, however, be divided into two groups: intragranular i.e. they precipitate within the grains, or intergranular, i.e. they are found at grain boundaries. Intragranular phases usually strengthen the grains, while grain boundary precipitates improve the creep resistance of the alloy [18]. The coming sections give a quick description of each type of precipitate.

## 2.2.2 Intragranular precipitates

**The  $\gamma'$  phase:** The most common type of strengthening precipitate is the  $\gamma'$  phase [2], which can be found in alloys like Waspaloy, René 42 and the alloy covered in this thesis, Haynes 282. It forms with the addition of Ti and Al into a ordered  $L1_2$  structure with a nominal chemical composition of  $Ni_3(Al,Ti)$ . In  $\gamma'$  strengthened alloys, it is the  $\gamma'$  precipitates that give the highest strengthening contribution. For some high fraction  $\gamma'$  alloys, large, primary  $\gamma'$  at grain boundaries are also employed during forging to control the grain size. Otherwise it is purposefully nucleated and grown during heat treatments employed post the thermomechanical processing steps.

**The  $\gamma''$  phase:** With addition of Nb to the alloy, the  $\gamma''$  phase can form. This phase is found in alloys like IN718 and IN706 [1].  $\gamma''$  phase has an ordered bct crystal structure with a nominal chemical composition of  $Ni_3Nb$ . Like  $\gamma'$ ,  $\gamma''$  is coherent with the matrix but has an anisotropic misfit with a maximum of 2.9 %. Their morphology is usually disc like. This phase is metastable and can transform to its stable form  $\delta$  during long term service at high temperatures.

**Carbides:** Carbides and borides also form inside the grains of Ni-base superalloys. Primary MC carbides exist throughout the matrix and appear as large, square or blocky particles. In superalloys, the metallic elements found in them are usually Ti, Cr and W. These carbides are unavoidable, as they nucleate

during solidification, with size, morphology and amount affected by the solidification conditions [19]. Due to their high dissolution temperature, they are not dissolved during processing and align themselves in lines, called stringers, during forming of the alloy.

**TCP phases:** The TCP (topologically closed packed) phases are undesired as they lower the overall ductility and mechanical properties of the alloy. They are in themselves brittle, but can also deplete the surrounding matrix of the solid solution strengthening elements [18]. Three different precipitates fall into the TCP phases, namely  $\sigma$  (tetragonal),  $\mu$  (rhombohedral) and laves (hexagonal). They appear after long time service, but can also nucleate during processing with an incorrect alloying content or non ideal processing steps.

### 2.2.3 Intergranular precipitates

**The  $\delta$  Phase:** In alloys that utilize  $\gamma''$  as their precipitation hardening particle (addition of Nb into the alloy), the  $\delta$  phase is precipitated during heat treatments, but can also appear in  $\gamma''$  strengthened alloys during service since  $\delta$  is the stable form of  $\gamma''$ . It has a needle like morphology and an ordered orthorhombic structure with chemical composition similar to  $\gamma''$  ( $\text{Ni}_3\text{Nb}$ ).  $\delta$  improves the dwell fatigue and notch sensitivity, but a higher amount of this phase can however lower the mechanical properties of alloys [20]. Forging is sometimes done below  $\delta$  solvus to have the  $\delta$  precipitates control the resulting grain size.

**The  $\eta$  phase:** This phase can be found in Ni-base superalloys that are precipitation strengthened by  $\gamma'$ , after long heat treatments between 600-850 °C, where the  $\gamma'$  breaks down and forms as  $\eta$  [21, 22]. but can also form at  $\gamma/\gamma'$  eutectic regions during solidification if the Ti/Al ratio is too high [23]. Its chemical composition is  $\text{Ni}_3\text{Ti}$  and exhibits a hexagonal crystal structure. In alloy Allvac 718+,  $\eta$  is used instead of  $\delta$  as a grain boundary strengthening precipitate [24], and is also studied to replace  $\gamma'$  [25] since it shows a higher thermal stability.

**Grain boundary carbides:**  $\text{M}_{23}\text{C}_6$  and  $\text{M}_6\text{C}$  are carbides that nucleate and grow at grain boundaries. M is usually Cr for  $\text{M}_{23}\text{C}_6$  and Mo for  $\text{M}_6\text{C}$ . The morphology of these carbides is dependent on the grain boundary type [17]. They are created in a controlled manner during heat treatments to improve the creep resistance of Ni-base superalloys by hindering grain boundary sliding.  $\text{M}_{23}\text{C}_6$  can also appear as stringers inside grains in alloy 625.

A summary of the chemistry and structure properties of all the mentioned phases can be found in table 2.1.

Table 2.1: Summary of phases in Ni-base superalloys.

Phase	Crystal structure	Chemical composition	Elements	Intra- or intergranull
$\gamma$	fcc (disordered)		Ni, Co, Fe, Cr, Mo, W	N/A
$\gamma'$	fcc (ordered L1 <sub>2</sub> )	Ni <sub>3</sub> (Al, Ti)	Ni, Al, Ti	Intra
$\gamma''$	bct (ordered D0 <sub>22</sub> )	Ni <sub>3</sub> Nb	Ni, Nb	Intra
MC	fcc	(Ti, Ta, Nb, Hf)C	Ti, Ta, Nb, Hf, C	Intra
$\delta$	orthorhombic (ordered Cu <sub>3</sub> Ti)	Ni <sub>3</sub> Nb	Ni, Nb	Inter
$\eta$	hcp (D0 <sub>24</sub> )	Ni <sub>3</sub> Ti	Ni, Ti	Intra
M <sub>23</sub> C <sub>6</sub>	complex cubic	(Cr, Fe, W, Mo) <sub>23</sub> M <sub>6</sub>	Cr, C	Intra
M <sub>6</sub> C	fcc	Mo <sub>6</sub> C	Mo, C	Intra
$\sigma$	tetragonal	FeCr, FeCrMo, CrCo	Fe, Cr, Mo, Co	Inter
$\mu$	rhombohedral	(Fe, Co) <sub>7</sub> (Mo, W) <sub>6</sub>	Fe, Co, Mo, W	Inter
Laves	hexagonal	Fe <sub>2</sub> Nb, Co <sub>2</sub> Ti, Fe <sub>2</sub> Ti	Fe, Co, Ti, Nb	Inter

## 2.3 Haynes 282

Haynes 282 is a relatively new, wrought,  $\gamma/\gamma'$ Ni-base superalloy, with a chemical composition shown in table 2.2. It was developed by Haynes International as a competitor for similar alloys like Waspaloy and René 41 [3]. Compared to these alloys, the  $\gamma'$  content is lower, having an equilibrium fraction of around 20 % in the fully heat treated condition. It was created as an alternative to alloys like Waspaloy with improved weldability and fabricability, which it receives from its slow kinetics of  $\gamma'$  growth.

Table 2.2: Chemical composition (wt%) of Haynes 282 according to material certificate.

Chemical composition of Haynes 282											
Element	Ni	Cr	Co	Mo	Ti	Al	Fe	Mn	Si	C	B
Composition	bal	19.3	10.2	8.7	2.2	1.5	0.9	0.05	<0.05	0.06	0.004

The primary phase in Haynes 282 is the solution strengthened  $\gamma$  matrix with a uniform distribution of  $\gamma'$  precipitates. The unit cells for both  $\gamma$  and  $\gamma'$  are presented in figure 2.1 (a,b).

Three types of carbides are precipitated in Haynes 282: MC, M<sub>6</sub>C and M<sub>23</sub>C<sub>6</sub>. The unit cells for each carbide are shown in figure 2.1 (c-e), and figure 2.2 shows the carbides in the microstructure of Haynes 282. MC (primary) carbides appear large and blocky inside of grains. The alloying elements shown in table 2.2 and EDS analysis in figure 2.2 (b) suggest that their chemical composition is (Ti, Mo)C. Due to their high dissolution temperature, they are always present. Other than being unavoidable, they do not contribute to the strength of the alloy as they are too few to hinder dislocation movement. They have, however, been seen to act as nucleation sites for particle stimulated nucleation during dynamic recrystallization of Haynes 282 [26] and can hinder grain growth in late stages of secondary recrystallization [27, 28]. The secondary carbides,

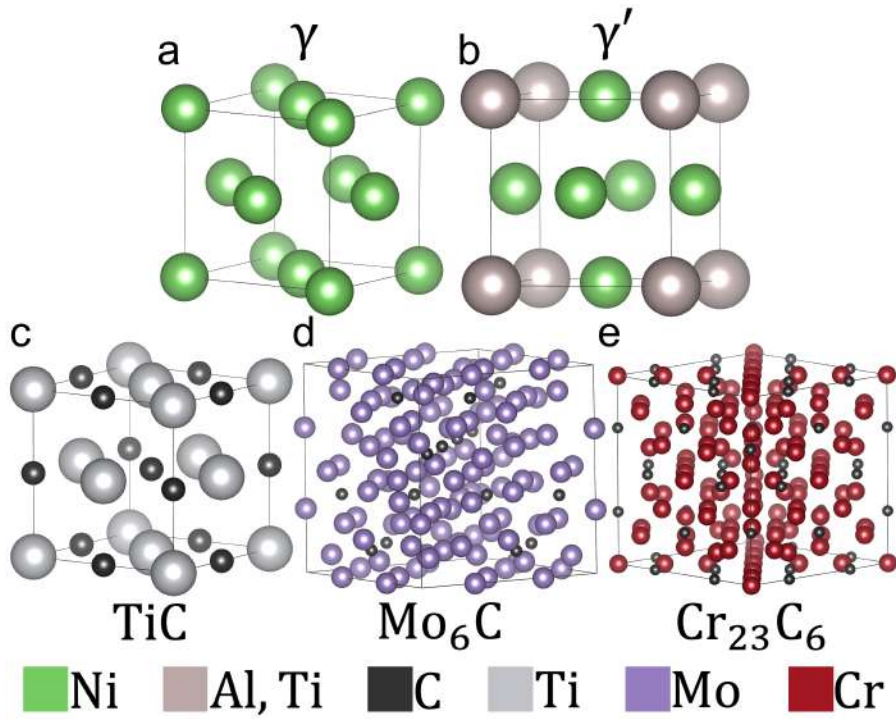


Figure 2.1: Representations of the unit cells for each phase in Haynes 282. a) shows  $\gamma$ , b)  $\gamma'$ , c) MC carbides, d)  $M_6C$  carbides and e)  $M_{23}C_6$  carbides. The illustrations were acquired from the The Materials Project database.

$M_6C$  and  $M_{23}C_6$ , are primarily located at grain boundaries. Carbide solvus for these are around 1100 °C [29]. In Haynes 282 their chemical composition is mainly  $Cr_{23}C_6$  and  $Mo_6C$  [4, 29–31], figure 2.2 (b). The morphology of the  $M_{23}C_6$  and  $M_6C$  carbides depend on the type of grain boundary they nucleate at. The higher the interfacial energy of the boundary, the easier a GB carbide can nucleate and grow, going from plate like to a triangular shape. At coherent  $\Sigma 3$  boundaries, they do not nucleate at all [32, 33]. All temperatures investigated in this work are above the  $\gamma'$  solvus so no  $\gamma'$  was present. The  $\gamma'$  precipitates, as well as grain boundary carbides, nucleate, by diffusional transformation [34, 35], and grow during heat treatment of Haynes 282, which are shown in figure 2.3. The first step, at 1100 °C, is a solution treatment where secondary particles (except MC carbides) are dissolved. The second step, first ageing step, performed at 1010 °C is done to nucleate the wanted hardening precipitates. The last step, the second ageing, at 788 °C grows these precipitates to their desired sizes and morphologies. During heat treatment carbon is supplied to grain boundary carbides from the matrix, but during longer thermal exposures, e.g. service, primary MC carbides break

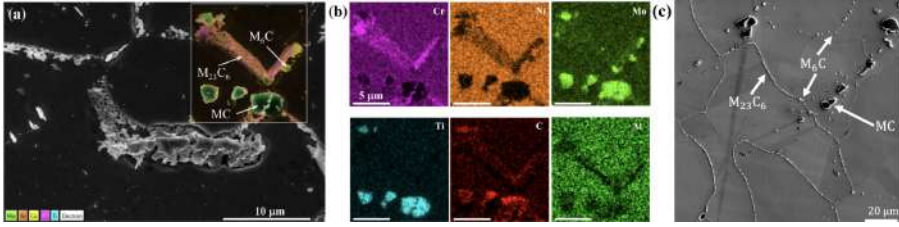


Figure 2.2: a) and b) show carbide structure, with corresponding EDS analysis for Haynes 282 aged at 800 °C for 98 hours [29] (used with permission). c) show carbide structure for Haynes 282 soaked for 30 min at 1080 °C, and can be regarded as the relevant structure for this work.

down according to the reactions shown in equations 2.1 and 2.2 supplying more carbon [27]

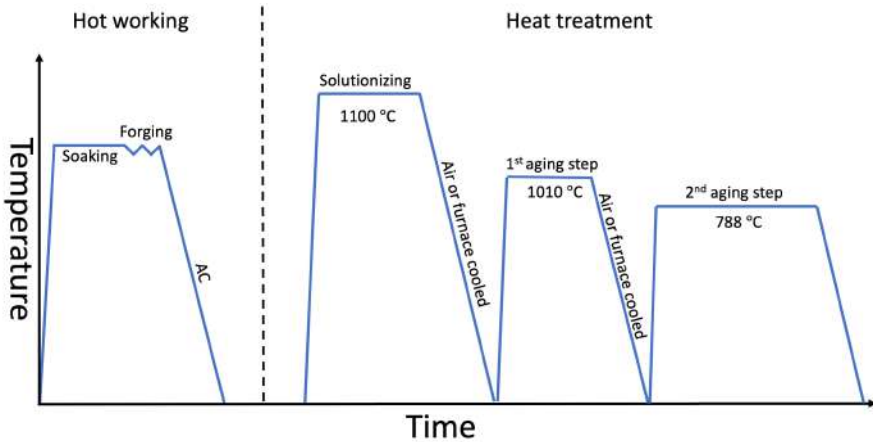


Figure 2.3: Standard thermo-mechanical procedure for Ni-base superalloys. Hot working constitutes forging procedures. Heat treatment show the three heat processing steps employed.

## 2.4 Hot working

Hot working is the name for a collection of manufacturing processes for metals and alloys, with high yield strengths, where the material is shaped to its

desired shape. For materials like Ni-base superalloys, shaping at elevated temperatures is necessary due to the high strengths and low fabricability at lower temperatures.

Typical processes that categorizes as hot working are e.g. hot rolling, extrusion and forging, usually done in multiple steps with intermittent annealing steps in between. A subsequent heat treatment where the material is again subjected to elevated temperatures but without deformation, called annealing or ageing are also common.

A typical hot working procedure for Ni-base superalloys is presented in figure 2.3. It consists of an initial soak of the billet in order to dissolve unwanted precipitates obtain a homogenous temperature throughout the piece. The second step is forging, where the piece is shaped to its desired shape. Depending on the size of the pieces, it can take a significant time for the it to cool.

The microstructure defines the properties of the finished metal/alloy. However, improving one property usually decreases another. In order to increase low cycle fatigue, a microstructure consisting of small grains is required. But smaller grains decreases the creep properties, due to the increase in total grain boundary length per unit volume. Knowledge about, and control of, the resulting microstructure is an extremely important aspect of manufacturing and developing components. Multiple parameters determine the resulting microstructure of the forged piece, e.g. deformation temperature, strain rate, total strain and cooling rate. The phenomena that drives the microstructural evolution at the higher strains employed during forging, is called recrystallization, and it is explained in the next chapter.

## Forging

Forging is defined as the process of deforming the material by compressive forces and is one of the oldest know metalworking techniques. The force applied is high enough to induce plastic deformation to shape the component. The force applied during forging also drives the change for the materials microstructure, which in turn changes the properties of the metal/alloy. Forging offers control both over shape and structure, with minimal loss of material. It is therefore of utmost importance to understand how each metal/alloy behaves by each forging parameter.

For Ni-base superalloys, the most common type of forging operations are open and closed die forming and ring rolling [36].

**Open die forming:** This is suitable as an initial forging operation for the creation of disks. The method is presented in figure 2.4 (a). The dies are

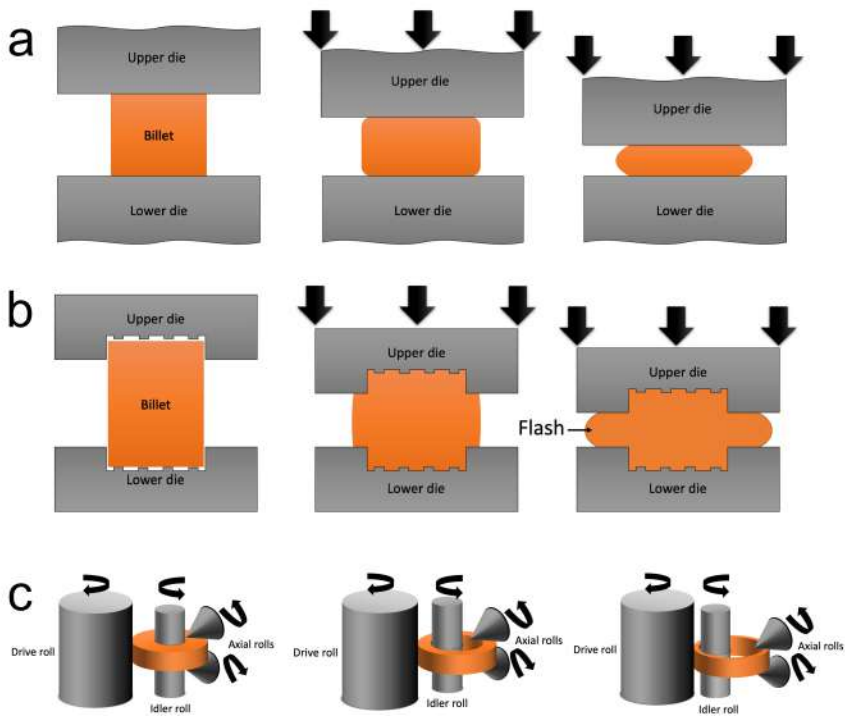


Figure 2.4: The most common forging operations for Ni-base superalloys. (a) open die forming, (b) closed die forming, (c) ring rolling.

open and the upper die is connected to a hydraulic press or hammer [37]. The finished component is called a pancake.

**Closed die forming:** For components with a more complicated geometry need a closed die. The closed die acts like a mold while a hammer or hydraulic press presses the metal/alloy to fill all cavities of the closed die. Excess material is ejected from smaller openings in the dies, called flash. This process is more expensive compared to open die forming because the dies need to be machined to get their desired shapes. The principle is shown in figure 2.4 (b).

**Ring rolling:** In order to create large casings for jet engines with often complex geometries, ring rolling is a suitable forging procedure. The initial preform is disc shaped with a hole in the middle. It is then rotated with rolls applying pressure to shape the spinning piece, figure 2.4 (c).

## CHAPTER 3

---

### Recrystallization

---

Recrystallization is defined as the phenomenon where strained and deformed grains in polycrystalline materials are replaced by new, dislocation free grains. This process occurs as a means to lower the internal energy of the material that has been induced through plastic deformation [38, 39]. Recrystallization can occur both statically, static recrystallization (SRX), and during an ongoing plastic deformation, dynamic recrystallization (DRX). Both occur at elevated temperatures where the former initiates statically during annealing to decrease the stored energy induced from cold working. The latter, on the other hand, occurs during hot working in order to reduce the increased energy from the ongoing plastic deformation.

Both SRX and DRX can in themselves be divided into two different phenomena, continuous (cSRX/cDRX) and discontinuous (dSRX/dDRX), with the main distinction that the discontinuous processes have a clear nucleation and growth stages, being described as a two stages process [39], while the continuous processes create a recrystallized microstructure uniformly throughout the specimen with no clear initiation step.

Since hot working is the subject for this thesis, only dynamic recrystallization will be further expanded upon in the rest of this chapter.

### 3.1 Dynamic recrystallization and mechanical response

Dynamic recrystallization is, as mentioned, occurring during plastic deformation at elevated temperatures ( $> 0.5T_m$ ) [39]. When a metal or alloy is plastically deformed, the atomic planes glide across each other through the movement and generation of dislocations. These 1D defects exert a local elastic strain by distorting the atomic planes in their vicinity. These strains interact, if the dislocations are in proximity, exerting repelling forces on each other. Therefore, dislocation movement becomes harder with an increasing density of dislocations  $\rho_d$ . The energy from this increase in  $\rho_d$  is given by

$$\rho \sim 0.5\rho_d Gb^2 \quad (3.1)$$

where  $G$  the shear modulus of the material and  $b^2$  is the magnitude of the burgers vector for dislocations.

The generation of dislocations is highest at the early stages of deformation and an increase in flow stress with applied strain, called work hardening, is seen as illustrated in figure 3.1. How this increase in dislocation density progresses, is mainly governed by the materials stacking fault energy  $\gamma_{SFE}$  which gives the probability of a dislocation dissociating into partials when moving through a grain. Dislocations in materials with low to medium  $\gamma_{SFE}$  have a higher tendency to dissociate partials because the resulting stacking fault will have a low enough energy to allow this. However, partial dislocations have a reduced ability to cross slip and climb, which result in restricted movement. Materials with high  $\gamma_{SFE}$  do not exhibit dissociations of dislocations, to the same extent, since the resulting stacking fault will have a high energy, making it energetically unfavourable for dislocations to dissociate. This unrestricted movement results in higher levels of annihilation and arrangement into substructures of dislocations, a process called dynamic recovery (DRV).

With further deformation, high  $\gamma_{SFE}$  materials, where DRV is prominent, will experience a decreased rate of work hardening when DRV initiates and eventually reach a steady state, where the work hardening from an increase in  $\rho_d$  and softening from DRV that lowers  $\rho_d$  balance each other, as shown in figure 3.1 (a). Low  $\gamma_{SFE}$  materials, where DRV cannot counter work hardening,  $\rho_d$  will continue to increase up to a point where the stored energy is high enough to initiate dDRX. In the stress-strain curve this is seen as a decrease in the work hardening rate up to a maximal stress  $\sigma_p$ , followed by a softening before a steady state is reached, figure 3.1 (b).

The  $\gamma_{SFE}$  of a material is, therefore, a governing parameter whether the recrystallization phenomena will be cDRX or dDRX. Commonly, low to medium  $\gamma_{SFE}$  materials are said to dynamically recrystallize through dDRX and materials with high  $\gamma_{SFE}$  through cDRX. The higher  $\rho_d$  in low to medium  $\gamma_{SFE}$

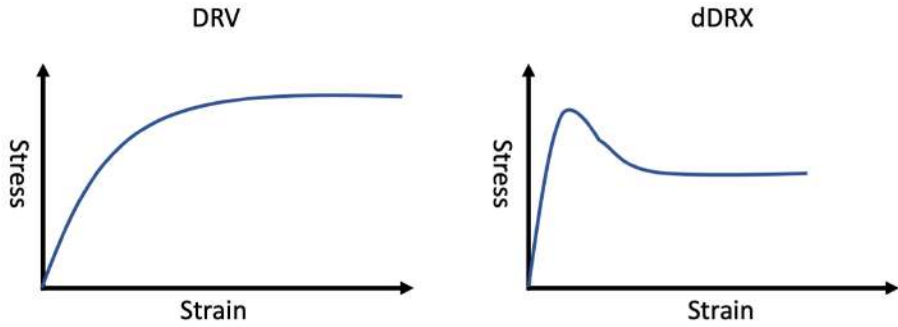


Figure 3.1: Mechanical response on hot deformation for a material with (a) high  $\gamma_{SFE}$  and (b) low  $\gamma_{SFE}$

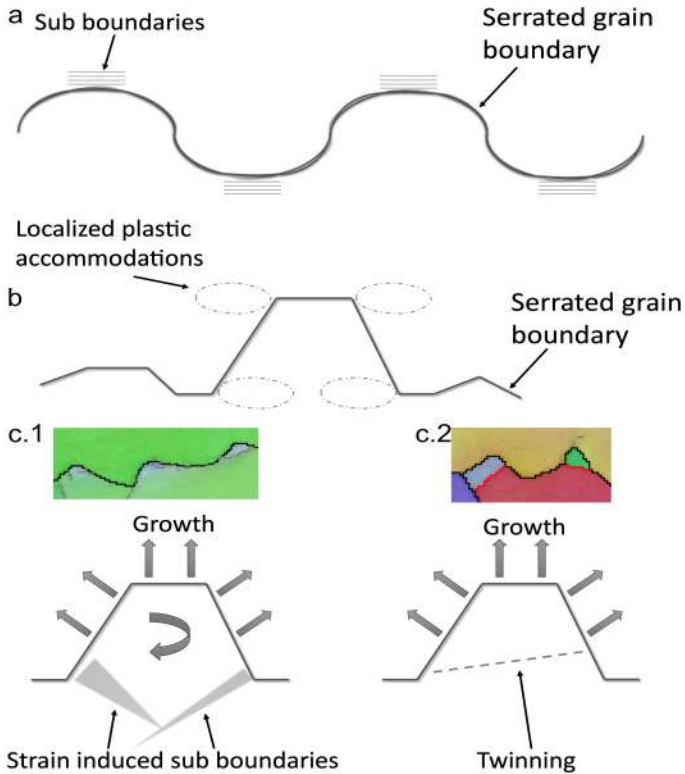


Figure 3.2: dDRX nucleation where (a) illustrates a sheared, serrated grain boundary with sub boundaries accumulating. (b) bulge of grain boundary, showing dDRX nucleus with localized plastic strain accommodations. Nucleus is cut off from parent by either (c.1) strain induced sub boundary (gray lines) or (c.2) twinning (red lines).

materials can generate the large local strains to initiate the nucleation. Dislocations move through the grains but cannot pass grain boundaries into other grains, due to the large mismatch in grain boundaries, so they will accumulate, creating high local strains, seen as bulging/serrations of grain boundaries with creation of sub-boundaries, illustrated in figure 3.2 (a). With further deformation, localized strains will accumulate along bulges, figure 3.2 (b), where new grains nucleate. The new dDRX grain is cut off from the parent grain, and grow into the other one, either by strain induced sub-boundaries evolving into high angle grain boundaries (HAGB), figure 3.2 (c.1) or by the creation of a twin boundary through a stacking fault, figure 3.2 (c.2). The former is more common during deformation at lower temperatures and higher strain rates, while the latter at higher temperatures and lower strain rates [38]. Nucleation during dDRX mainly occurs at grain boundaries, [40], and the term "necklace structure" is often used since the deformed grains become surrounded with recrystallized grains, figure 3.3 (a), that can easily grow at the expense of the deformed grains. Since HAGB between the deformed and recrystallized grain is so unstructured, atoms in the boundary can easily arrange themselves in the structure and orientation of the growing grain.

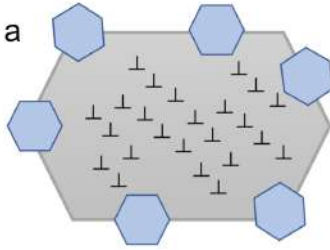
Large ( $> 1 \mu\text{m}$ ) secondary particles can also act as nucleation sites, a process called particle stimulated nucleation (PSN) [41–43]. A high local  $\rho_d$  accumulates at these particles, creating misorientations by sub boundary accumulation into HAGB [43].

cDRX, on the other hand, does not have a clear nucleation stage but instead occur through arrangement of dislocation into networks. Continuous generation of dislocations through further deformation fuels these networks to become low angle grain boundaries (LAGB) and in the end become HAGB. This happens throughout the deformed grains which gradually transform into a recrystallized structure, as shown in figure 3.3 (b). Often this requires much higher strains [44], due to DRV countering the generation of dislocations. These strains cannot be accomplished in compression or tensile testing, so stress-strain curves displaying cDRX are not readily available [38].

The distinction between cDRX and dDRX can be seen in the grain boundary structure of the material at different strains. Because cDRX is a continuous process where LAGB evolve into HAGB throughout the deformed grains, cDRX lead to an increase in LAGB. dDRX on the other hand does not develop the substructures of LAGB so the LAGB count will remain relatively stable. It should be noted however that a slight increase in LAGB will be seen in either case due to dislocation build up during work hardening [45]. DRV occurs in all materials to varying extents and only includes reduction in stored energy by dislocation movement [46], and not movement of any grain boundaries.

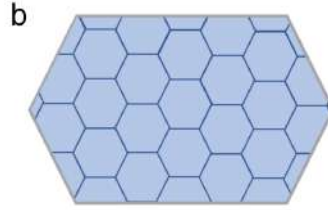
If the sample is not fully recrystallized after deformation, and the material is

### Discontinuous dynamic recrystallization



Necklace structure: new grains nucleate and boundaries of old grains

### Continuous dynamic recrystallization



Creation of substructures that evolve into HAGB throughout old grains

Figure 3.3: Illustration over dDRX (a) and cDRX (b). During dDRX, a necklace structure is seen where new grains recrystallized at grain boundaries of deformed ones. During cDRX, dislocations create substructures inside grains, and eventually evolve into HAGB.

not quenched, recrystallization will continue without deformation. This process is called meta-dynamic recrystallization (mDRX), defined as the continued growth of the recrystallized grains. It has no incubation time since nucleated grains already exist, and occurs immediately after deformation [39, 47]. In cold worked materials discontinuous static recrystallization, dSRX, can occur if the material is annealed. The high stored energy from the cold working can, together with the thermal energy, drive nucleation and growth of grains, [39]. Both mDRX and dSRX occur in materials with low to medium  $\gamma_{SFE}$ , i.e. where recrystallization occurs through a clear nucleation - growth process. If materials where cDRX occur are annealed after being cold worked, they continue to recrystallize through cSRX, which is a rearrangement of dislocations [39].

The growth of nucleated grains during dDRX and mDRX, into remaining deformed grains, occurs to further decrease the stored energy form  $\rho_d$ . Because new grains nucleate from deformed ones through the serrations/bulging of grain boundaries, their orientation have a higher probability to be similar to their parent grain. It has also been shown that nuclei with the same orientation as their parent are more likely to grow through HAGB movement compared to nuclei with other orientations [46]. HAGBs move through diffusion where atoms diffuse from the deformed grain into the GB and from the GB into the recrystallized grain.

In fcc metals, many of the HAGB that form during recrystallization are, or become, coincident site lattice (CSL) boundaries [48, 49]. The main form of these is the  $\Sigma 3$  type boundary, called twin boundaries. They form both during

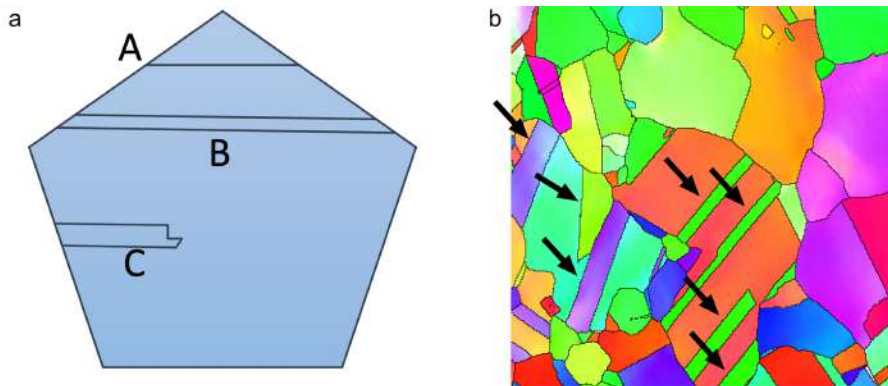


Figure 3.4: (a) Different morphologies of annealing twins in fcc crystals. (b) microstructure with grains containing many annealing twins. Color is determined by grain orientation.

nucleation and growth of grains through different processes. One way of twin creation is called growth accident formation where the stacking sequence of  $\{111\}$  planes experiences a stacking fault during growth, i.e. the ordering of the crystal planes becomes ..ABCABACABC.. [50]. They usually form at triple junctions, see A in figure 3.4 (a). These boundaries have a very low energy compared to random HAGB. Another mechanism for describing the formation of annealing twins are stacking faults terminated by partial dislocations, C in figure 3.4 (a).

During uniaxial hot compression, fcc materials experience a texture evolution where the deformed grains take on a  $\langle 110 \rangle$ -fiber texture due to progressive rotation of  $\langle 110 \rangle$  towards the compression axis [51]. During dDRX the recrystallized grains adopt this texture to a certain extent and a, weaker,  $\langle 110 \rangle$ -fiber texture is visible in the recrystallized fraction. Interestingly, this process is not seen during PSN, where the texture of the recrystallized grains is random [26, 43]. However, since annealing twins form prominently during recrystallization and grain growth, the texture becomes random. Twins, having a  $60^\circ \langle 111 \rangle$  rotation compared with the orientation in the grain it forms, reduce the texture adopted from the parent grains, figure 3.4 (b). Higher order twins can also form when twinning occurs in primary twins [49] where multiple family of twins evolve in one grain.

### 3.2 Dynamic recrystallization in Ni-base superalloys

Ni-base superalloys generally have a low to medium  $\gamma_{SFE}$  [52–54], and the primary mode of dynamic recrystallization observed is dDRX [55–57]. However

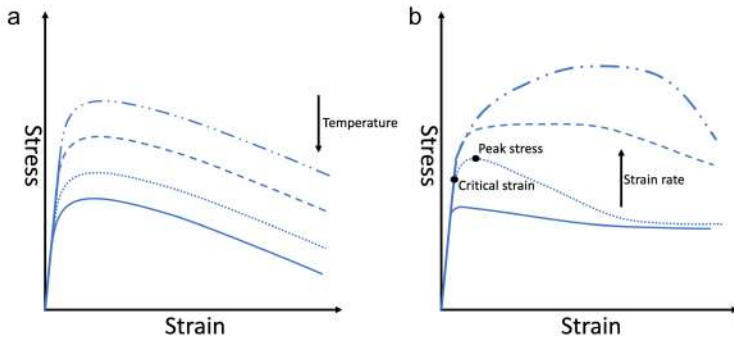


Figure 3.5: The effect of deformation parameters on the mechanical response of Ni-base superalloys. (a) strain rate, (b) temperature.

some suggest that cDRX also can occur at lower deformation temperatures and higher strain rates [45, 56–58], as well as at the initial stages of deformation to later be replaced by dDRX [59]. Multiple dynamic recrystallization phenomena has been seen for different materials [38].

Figure 3.5 shows the typical appearances and changes in the stress-strain response for Ni-base superalloys with varying deformation parameters, where (a) illustrates different temperature and (b) different strain rates. The critical strain marked is given as the onset of DRX, which leads to a decreased work hardening rate. The peak stress is the maximum stress after which a flow softening is often observed prior to achieving a steady state flow, after which the hardening and softening rate are in equilibrium and the stress remains constant. Since dDRX contains thermal elements [39], a higher temperature helps drive the recrystallization. Deforming at higher temperatures also increases the occurrences of other thermal processes like flow, so with increasing deformation temperature, the measured flow stress decreases, figure 3.5 (a) [55, 60].

With an increase in strain rate, figure 3.5 (b) the generation of dislocation is faster, leading to a higher  $\rho_d$ , while time for DRV decreases, leading to a higher work hardening, and the peak stress occurs at larger strains due to the faster deformation [55]. Increasing the strain rates also leads to a higher adiabatic heating [56]. This is the explanation for the faster softening rate seen at higher strain rates, figure 3.5 (b). This increase in thermal energy helps soften the material by a higher diffusion rate of vacancies and mobility of dislocations [14]. It also increases the mobility of HAGB increasing growth rate of DRX grains which softens the material.

Zhang et al. [61] investigated the dynamic recrystallization mechanisms in a Ni-base superalloy and found that for their deformation parameters (1010 °C-

1210 °C), and a strain rate of  $0.1 \text{ s}^{-1}$  the flow stress decreased with increasing temperature. The onset of DRX was found to occur at smaller strains with increasing temperature due to the higher dislocation mobility. Zhang et al. [62] also investigated the evolution of recrystallization with strain. They found that DRX had occurred at a strain of 0.1. The increase in recrystallized fraction was most intense between strains of 0.1 and 0.3 where the fraction increased from 0.05 to above 0.5. Interestingly, when comparing with the average grain sizes of recrystallized grains the largest increase occurred between strains of 0.3 and 0.5 where the average size increased from 6 to 15  $\mu\text{m}$ . This is a clear indication of dDRX where grains first nucleate, and then grow.

Azarbarmas et al. [57] investigated Inconel 718 over multiple strains (0.2, 0.4, 0.7), strain rates ( $0.001\text{-}1 \text{ s}^{-1}$ ) and temperatures (950-110 °C). They showed a similar mechanical response as the one illustrated in figure 3.5. The flow stress decreased with increasing temperature and decreasing strain rate, and the peak stress occurred at lower strains with decreasing strain rates. They also found that nucleation occurred through twin boundaries "cutting off" the grain boundary bulges, as illustrated in figure 3.2 (c.2). They also noted that boundaries lost their  $\Sigma 3$  characteristics, however, during growth of grains new twins generated. This suggests multiple processes for formation of  $\Sigma 3$  twin boundaries in Ni-base superalloys.

Deforming at high temperatures and low strain rates reduces the observed flow softening prior to steady state flow. Kumar et al. [54] showed that when deforming at 1150 °C, with a strain rate of  $10^{-4} \text{ s}^{-1}$  a steady state in the stress-strain curves were achieved without a flow softening, indicating that DRV has a more prominent role in these deformation regimes, which was attributed to the long deformation times. The increase in flow softening at higher strain rates, up to  $1 \text{ s}^{-1}$ , was explained by the increase in adiabatic heating which softened the material. This effect was also shown by D'Souza et al. [63] for deformation at 1140 °C with a strain rate of  $0.1 \text{ s}^{-1}$  as well as Zhang et al. [56] who measured the critical strain rate to  $1 \text{ s}^{-1}$  when deforming at 1110 °C.

During dynamic recrystallization of Ni-base superalloys, the recrystallized fraction often display a minima at intermediate strain rates. Kumar et al. [54] showed this phenomena in their study, where the lowest DRX fraction was for a strain rate of  $0.01 \text{ s}^{-1}$  when deforming at 1150 °C to a total strain of 0.7. Nicolay et al. [64] states that the DRX fraction is dependent on strain rate, and there exists an intermediate strain rate where the DRX will be at a minimum, termed "critical strain rate". This can be seen for the three strain rates deformed at 1080 °C. It is however also possible that this effect is temperature dependent and shifts to higher strain rates for lower deformation temperatures, since dDRX is a temperature dependent process and the added driving force from adiabatic heating at higher strain rates becomes less impactful at lower deformation temperatures.

# CHAPTER 4

---

## Experimental Methods

---

### 4.1 Thermomechanical deformation

#### 4.1.1 Sample preparation

Haynes 282 was supplied as discs with a diameter of 152 mm (6 inches) and thickness of 15 mm cut from a billet. From these disks, samples for hot compression testing using Gleeble were prepared by electric discharge machining (EDM) in a circle at half the radius of the disks, so that the initial microstructure would be homogenous. The finished samples were in the form of cylinders with dimensions  $\varnothing 8$  mm and 12 mm in length. An illustration is shown in figure 4.1. The disks were flat milled to create good parallelity between the upper and lower side. The samples were then cut out by electric discharge machining (EDM) and turned to a diameter of 8 mm.

#### 4.1.2 Gleeble

The Gleeble system is a thermomechanical simulator. It is able to perform both compression, tensile and cyclic testing over a large variety of heating rates and

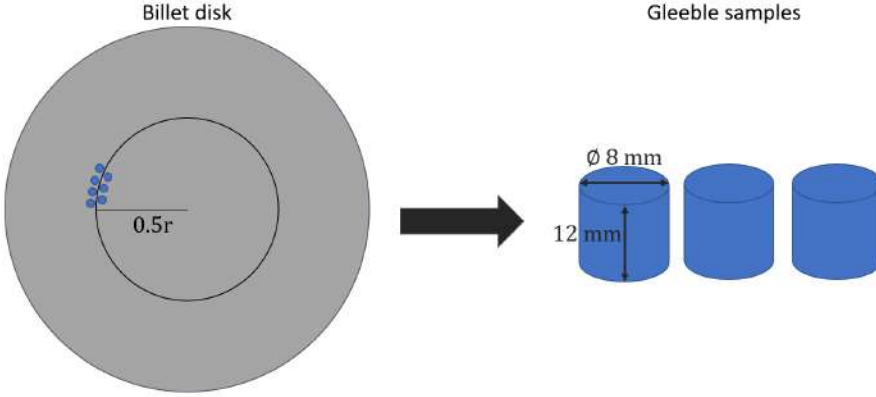


Figure 4.1: Illustration over creating of the Gleeble samples.

deformation parameters [65, 66]. Thanks to this, it is ideal to simulate forging operations. To control the temperature, a thermocouple is spot welded to the sample, which is then placed between two anvils, shown in figure 4.2. The samples is then heated resistively. When the target temperature is reached, some time is given to let the temperature stabilize and even out throughout the sample prior to deformation. Too large heating gradients can lead to uneven deformation, shown in figure 4.2 (b). Another undesirable feature from the Gleeble testing is barrelling. This occurs because the flow will be inhomogeneous throughout the volume. The flow will be highest at the central region of the sample volume, while due to friction, it will be lower at the anvil interfaces [67]. Uneven deformation is undesirable, since the result will destroy the reproducibility of the testing as well as create an uncertainty of where the flow was largest. In order to avoid uneven deformation, a high tolerance for the parallelism between the flat sides of the sample is needed. The other parameter is to reduce the friction between sample and the anvils, so the sides are lubricated. For hot deformation this is usually graphite, borite or glass [68]. For these tests, thin sheets of graphite was placed between the sample and anvils.

The Gleeble registers the compressive force [kN], displacement of the anvils [mm], temperature from the thermocouple [ $^{\circ}\text{C}$ ] and time [s]. With the force and displacement, the true strain and true stress can be calculated with equation 4.1 and 4.2 respectively,

$$\epsilon = \ln\left(\frac{L_0 + \Delta L}{L_0}\right) \quad (4.1)$$

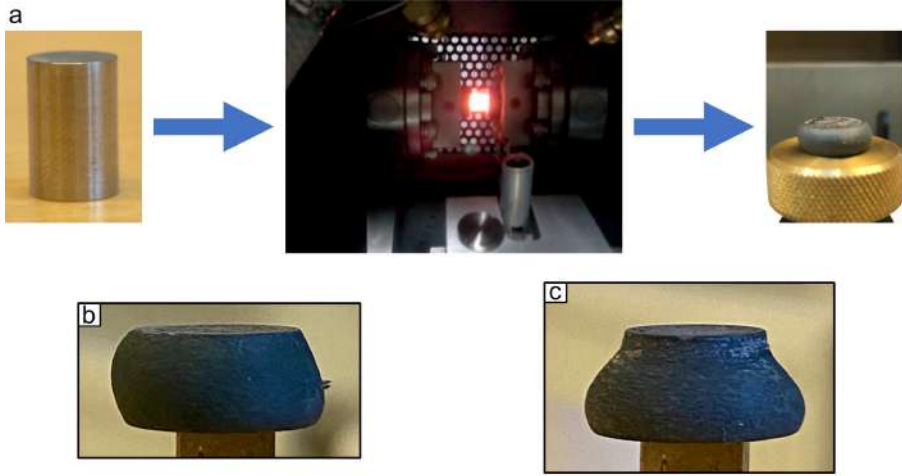


Figure 4.2: (a) Initial sample dimension, the Gleeble setup with a red hot sample right before compression, and the resulting compressed sample after quench. (b, c) show complications that can occur during hot compression where (b) shows uneven deformation and (c) uneven temperature.

$$\sigma = \frac{F}{A_0} * \frac{L_0 + \Delta L}{L_0} \quad (4.2)$$

where  $L_0$  is the initial gauge length,  $\Delta L$  the displacement,  $F$  the force and  $d_0$  the initial diameter of the sample. A fault in these equations is that they assume a uniform deformation throughout the volume, which has already been mentioned is not true. Finite element method (FEM), show that the distributions of temperature, strain [69] and strain rate, [70] throughout a sample during compression is inhomogeneous. Figure 4.3 show the effective strain in a Gleeble sample. Due to this, the exact values of temperature, strain and strain rate are not known, and the microstructures presented in later chapters are only representative for nominal conditions. To have comparative results, in despite of this, the examined microstructures were all form the centre of each sample volume.

The thermomechanical procedures employed in this thesis are illustrated in figure 4.4, and are divided into 3 different subsets. The first subset, figure 4.4 (a), contains samples soaked and deformed at the same temperature, either 1060 °C, 1080 °C (sub-solvus) or 1120 °C and quenched directly after deformation. The second subset, figure 4.4 (b), contains samples soaked at 1120 °C (above solvus) and deformed at 1080 °C (sub-solvus), and quenched directly after deformation. The third subset, figure 4.4 (c), contains samples soaked

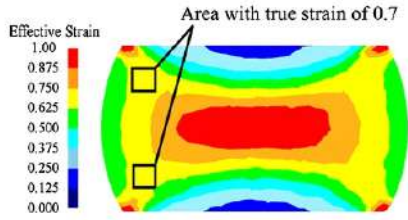


Figure 4.3: FEM simulations of the effective strain throughout the sample volume during hot compression to a true strain of 0.7 in a Gleeble. Acquired from [69] with permission.

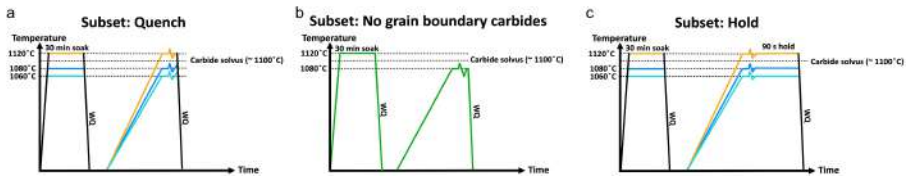


Figure 4.4: The thermomechanical procedures for each sample. (a) samples soaked and deformed at either 1060 °C, 1080 °C or 1120 °C and quenched directly after deformation. (b) samples soaked at 1120 °C and deformed at 1080 °C and quenched directly after deformation. (c) samples soaked and deformed at either 1060 °C, 1080 °C or 1120 °C and held for 90 s after deformation before being quenched.

and deformed at the same temperature, as subset 1, but were held at target temperature for 90 s after deformation before being quenched. The samples were soaked in a pre heated oven for 30 min and later dropped in water. In the Gleeble, all samples were heated over 60 s and held for 10 s before deformation in order to stabilize the temperature. This short holding time should not have caused significant precipitation of grain boundary carbides.

## 4.2 Microstructural characterization

### 4.2.1 Sample preparation

After the thermomechanical procedure in the Gleeble, in order to evaluate the microstructure of the centre of the sample volume, the samples were cut along the deformation direction in a Behler low speed saw. The cut surfaces were then encased in conductive Bakelite and mechanically ground with SiC paper with grits ranging from P300-P4000, polished with diamond particles of sizes

3, 1 and 0.25  $\mu\text{m}$  and lastly oxide polished with a colloidal silica suspension. The complete grinding and polishing procedure is shown in table 4.1. The force was over each individual sample and a co-rotation, meaning that both head and bottom were spinning in the same rotation, and counter-rotation for when they spinning in the opposite directions. Grinding papers were used for maximum 2 minutes before being changed. Diamond particles were supplied once every 30-60 s and oxide polishing suspension was constantly added slowly until 20 s of the polishing time remained, after which water was used to wash away the silica suspension. This resulted in a deformation free surface required for EBSD and ECCI analysis.

In order to see the GB carbides, samples were electro-etched in a solution of 98 ml HCl and 2 g oxalic acid at 3 V for 3-5 s at room temperature.

Table 4.1: Grinding and polishing procedure.

Grinding procedure				
Coarseness grinding paper	Time (min)	Force (N)	Rotation	Rotation speeds (head/bottom) (RPM)
P320	1	25	Co-rotation	150/300
P500	1	25	Co-rotation	150/300
P800	1	25	Co-rotation	150/300
P1200	2	15	Co-rotation	150/300
P2000	5	10	Co-rotation	150/300
P4000	6	10	Co-rotation	150/300
Polishing procedure				
Diamond particle size ( $\mu\text{m}$ )	Time (min)	Force (N)	Rotation	Rotation speeds (head/bottom) (RPM)
3	12	10	Co-rotation	150/300
1	12	10	Co-rotation	150/300
0.25	12	10	Co-rotation	150/300
Oxide polishing				
Oxide polishing	Time (min)	Force (N)	Rotation	Rotation speeds (head/bottom) (RPM)
Colloidal silica suspension 0.04 $\mu\text{m}$	15	10	Counter-rotation	150/300

## 4.2.2 Scanning electron microscopy

Scanning electron microscopy (SEM) is a microscope that uses electrons for illumination. A beam is created at the electron gun, focused with electromagnetic lenses and the different interactions between the electrons from the beam and the atoms in the sample are collected by a multitude of detectors. Due to the common knowledge of how SEM work, the basics will not be explained. The two main modes of operation used for the work presented in this thesis is electron channelling contrast imaging (ECCI) and electron backscatter diffraction (EBSD) which are explained below.

### Electron channelling contrast imaging

ECCI is a useful tool in the SEM to get information of the microstructure. If the surface is free from deformation, contrast from the backscattered electrons

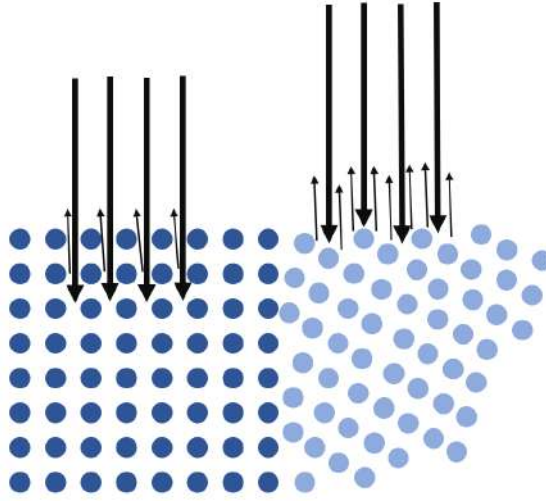


Figure 4.5: ECCI illustration showing the incoming electron beam as large arrows and the outgoing BSE as small arrows. The amount of BSE from each grain is dependent on its orientation.

are partially determined by the orientation of the grains with respect to the incident beam. When it enters the sample a primary wave field is created with the lattice. Due to the crystallinity of the material, long range order of atoms exists, which create a periodic variation of charge densities throughout the grain [71], illustrated as "channels" in figure 4.5. Depending on the orientation of the atomic planes of the lattice in the grain, the Bragg condition, see equation 4.3 can be fulfilled which causes diffraction of the incident beam. This makes the probability of backscattered electrons low. If, however, the Bragg condition is not met by the lattice, this probability increases, generating more backscattered electrons. Different orientations therefore cause differences in contrast and grains are easy to distinguish like seen in the ECCI image shown in figure 4.6. For samples containing deformed grains, the lattice orientations changes within the grain which is also visible in ECCI e.g. the deformation present at the left side along the upper edge in figure 4.6.

$$\lambda = 2d_{hkl} \sin \theta_{hkl} \quad (4.3)$$

The optimal parameters in order to conduct ECCI are to create as parallel a beam as possible while maintaining a high spatial resolution to minimize the escape area of the backscattered electrons [71], with highest possible current. ECCI is a surface sensitive technique (10-100 nm) since further penetration depth give rise to more scattering events which destroys the parallel electron beam

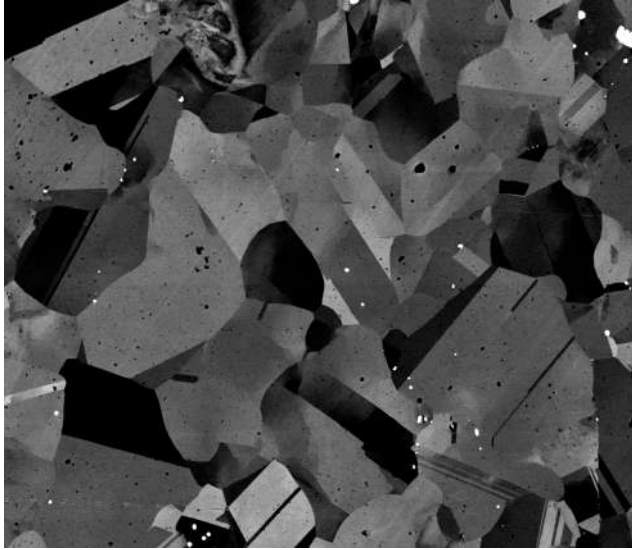


Figure 4.6: ECCI image showing the microstructure of H282 Ni-base superalloy.

### Electron backscatter diffraction

In order to fully understand the microstructure, and recrystallization phenomena occurring in the material, the crystallographic orientations of the grains have to be determined. EBSD offers a relatively good statistical picture, with an optimal spatial resolution, of the microstructure with information of each local orientation. EBSD is performed with a  $70^\circ$  tilt compared to the plane normal of the sample, as is illustrated in figure 4.7. Some electrons from the beam will scatter inelastically, which will change their energy to satisfy the Bragg condition, equation 4.3, at either  $+\theta$  or  $-\theta$  [71]. Another way to define it is to say that the inelastically scattered electrons create point sources inside the specimen, from which they are then elastically scattered through diffraction [72]. The diffracted electrons exit the surface of the material and hit a fluorescent screen where a Kikuchi pattern consisting of pair of lines, Kikuchi bands are formed. Figure 4.8 shows the corresponding Kikuchi bands from three different points (1, 2, 3) on a finely polished surface. Lines corresponding to the same band are electrons scattered from planes  $(hkl)$  and  $(\bar{h}\bar{k}\bar{l})$  and are actually a small section of a Kossel cone that contains crystallographic information of the material. The spacing between Kikuchi bands is proportional to  $2\theta$ , which in turn contains information about the interatomic spacing through Bragg's Law, equation 4.3.

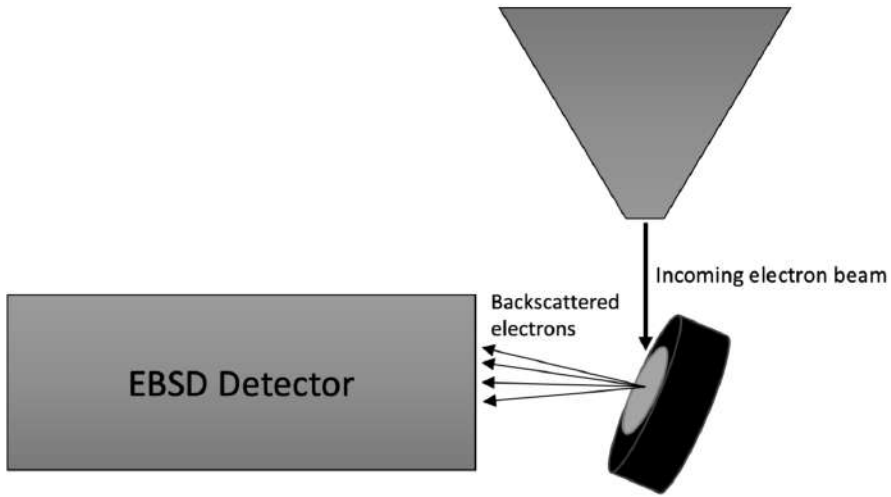


Figure 4.7: Illustration of EBSD setup in the SEM

The Kikuchi patterns are created on a fluorescent screen and captured by a CCD camera located behind it. Computer software can analyse these patterns and determine the crystallographic orientation of the specific point on the sample. The red cubes in figure 4.8 show the corresponding orientation of each point (1, 2, 3) based on the captured Kikuchi pattern.

From each pixel, information about the phase match, orientation values, quality metric, confidence of error and pixel position are saved. For faster acquisition the orientation values are saved as three Euler angles ( $\phi_1$ ,  $\Phi$  and  $\phi_2$ ), quality metric is saved as a mean angular deviation (MAD) value. When data has been collected, the maps can be recreated either in a stand alone software (like CHANNEL 5) or in MTEX [73], a Matlab extension.

Figure 4.9 shows different types of information that can be determined through the EBSD data. Figure 4.9 (a) shows the band contrast, which gives an indication of the quality of the data gathered. Since grain boundaries are not crystallographically ordered like the bulk of a grain, the signal from them is much worse, making them darker in the band contrast map. This results in a nice visualization over the microstructure. Figure 4.9 (b) is what is called an inverse pole figure (IPF) map. Here each pixel receives a colour, based on its orientation compared to some direction (often the direction of deformation), so the IPF map gives a good understanding about the orientation of the grains, if there exist a texture etc. EBSD is not only useful for determining crystallographic data, it can also give information of plastic deformation and strain by pattern rotation [74, 75]. Figure 4.9 (c) shows a grain reference ori-

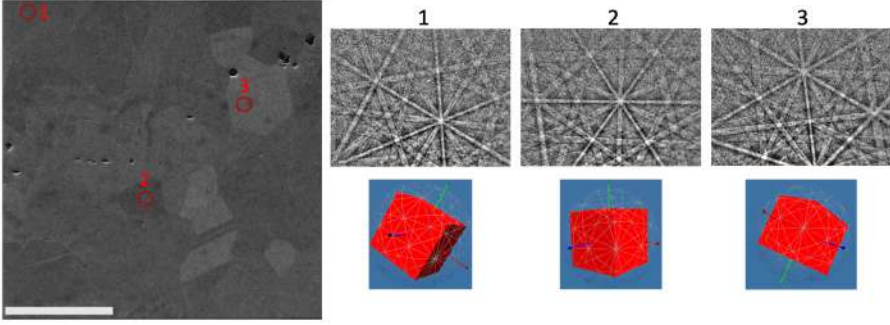


Figure 4.8: Leftmost: SE image with three positions marked. 1-3 the backscatter Kikuchi pattern for each position marked in SE image and the corresponding crystallographic orientation of the grains at each position.

entation deviation (GROD) map. The misorientation of each pixel in a grain is compared to the average orientation of the entire grain. The higher the misorientation, the higher the GROD value for that specific pixel. Figure 4.9 (d) shows a grain orientation spread (GOS) map where each grain is given a colour based on the spread of orientations for pixels in the grain, calculated with equation 4.4.

$$\text{GOS} = \frac{1}{N} \sum_{i=1}^N (|\Theta_i - \Theta|) \quad (4.4)$$

where  $N$  is the amount of pixels in a grain,  $\Theta_i - \Theta$  is the orientation difference between the current pixel  $\Theta_i$  and the average orientation of the grain  $\Theta$ . In order to inspect the strain more locally, the kernel average misorientation (KAM) map can be produced, figure 4.9 (e). A kernel is a small square of pixels,  $3 \times 3$ ,  $5 \times 5$ , ..., where the mean misorientation between the central pixel and its neighbours is calculated, with equation 4.5.

$$\text{KAM}_{i,j} = \frac{1}{|N(i,j)|} \sum_{(k,l) \in N(i,j)} \omega(o_{i,j}, o_{k,l}) \quad (4.5)$$

where  $N(i,j)$  is the number of all neighbouring pixels,  $\omega(o_{i,j}, o_{k,l})$  is the misorientation between the central pixel  $o_{i,j}$  and the neighbouring pixel  $o_{k,l}$ .

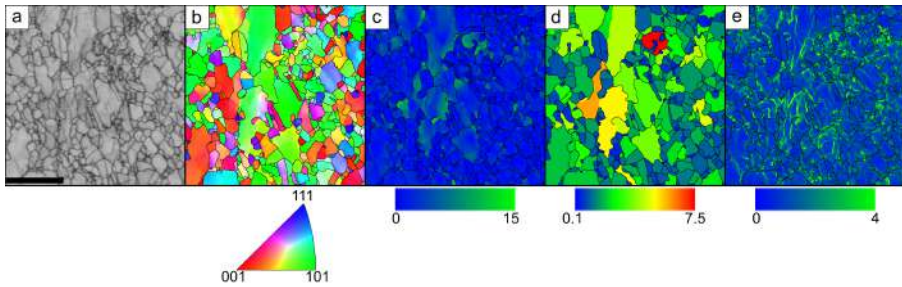


Figure 4.9: Possible data acquired with EBSD. a) band contrast, b) inverse pole figure, c) grain reference orientation deviation, d) grain orientation spread, e) local misorientation. Legend in b) shows colour to crystallographic orientation with respect to deformation direction, and c)-e) shows degrees. Scale bar in (a) is 20  $\mu\text{m}$ .

# CHAPTER 5

---

## Results and discussion

---

The work presented in this thesis evaluates the microstructural evolution of Haynes 282 during hot compression with different thermomechanical parameters. The mechanical data received from the Gleeble tests was correlated with the microstructural data obtained from the tested specimen by ECCI and EBSD.

First, the initial structure of the investigated material will be presented in section 5.1, with subsequent sections aim to answer the three questions asked in the introduction. Section 5.2 covers the dynamic recrystallization mainly focusing on temperatures below the sub solvus carbide temperature. What kind of dynamic recrystallization was observed, and what could be said in regards to deformation temperature and strain rate. Section 5.3 aims to answer the question of what the role of secondary carbides at grain boundaries have on the dynamic recrystallization when deforming at sub solvus temperatures. And finally section 5.4 covers the microstructural evolution during post dynamic recrystallization.

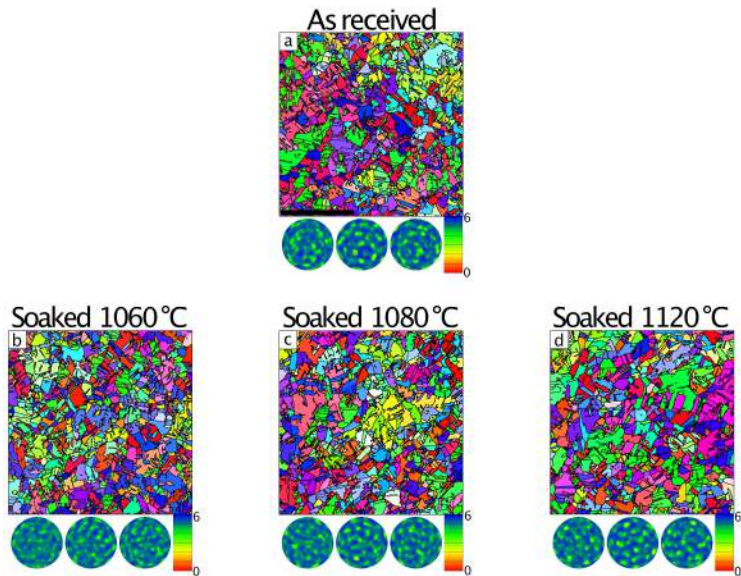


Figure 5.1: Inverse pole figure maps and pole figures for (a) as received structure, (b) soaked at 1060 °C for 30 min, (c) soaked at 1080 °C for 30 min and (d) soaked at 1120 °C for 30 min. Scale bar is 1 mm.

## 5.1 Initial structure

The as received, billet, microstructure is shown in figure 5.1 (a) and the microstructures after soaking for 30 minutes at each investigated temperature are shown in (b) 1060 °C, (c) 1080 °C and (d) 1120 °C. Each map spans an area of  $2.5 \times 2.5$  mm. The corresponding pole figures to each map show a random texture for all samples. Average grain sizes from each map were 150  $\mu\text{m}$ , figure 5.1 (a), 137  $\mu\text{m}$ , 5.1 (b), 177  $\mu\text{m}$ , 5.1 (c), and 179  $\mu\text{m}$ , 5.1 (d). Soaking for 30 minutes at any temperature did not alter the microstructure from the as received structure, so it can be safe to assume that each sample had a similar structure when being subjected to hot compression.

## 5.2 Dynamic recrystallization at sub-solvus temperatures

### 5.2.1 Mechanical response

The force–displacement Gleeble data, calculated and plotted as true stress–strain curves with equations 4.1 and 4.2, are shown in figure 5.2 (a-c), for samples WQ directly after deformation, and 5.2 (d-f) for samples held 90 s

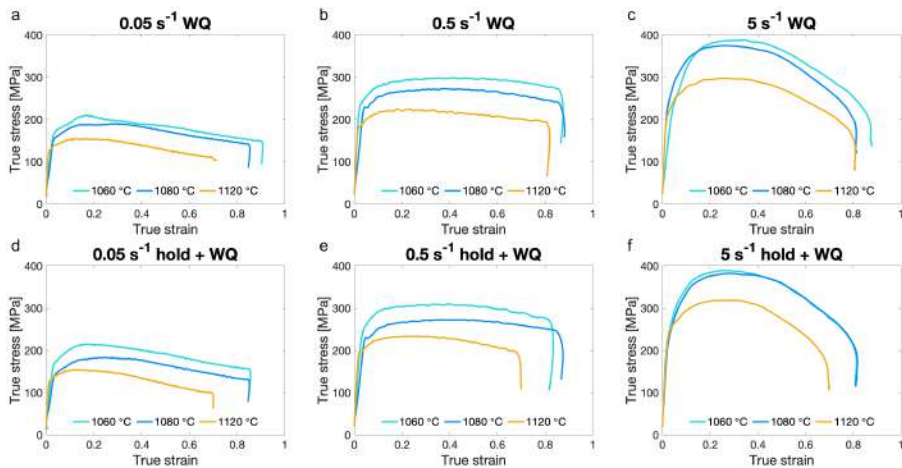


Figure 5.2: True stress–strain curves of samples deformed at  $0.05 \text{ s}^{-1}$ ,  $0.5 \text{ s}^{-1}$  and  $5 \text{ s}^{-1}$  with WQ directly after deformation (a - c). (d - f) for samples deformed at  $0.05 \text{ s}^{-1}$ ,  $0.5 \text{ s}^{-1}$  and  $5 \text{ s}^{-1}$  and held at 90 s prior to WQ.

prior to being quenched. The holding is static, and takes place after deformation, and does not affect the stress-strain curves that are portrayed in the graphs. Deformation under the same conditions yielded similar curves, figure 5.2, however, slight variations in measured stress levels for the same temperatures and strain rates was observed.

The initial stress response shows work hardening, which is an increase in  $\rho_d$  that hinders further deformation. When a critical strain is reached, the rate of working hardening start to decrease, and this is often considered to correspond to the initiation of dDRX. The work hardening rate continued to decrease up to the maximum stress, after which flow softening was observed. This indicated that the decrease in  $\rho_d$  from DRV and DRX outmatched the increase from further deformation. A steady state flow, where the contributions of the softening and strengthening effects are in equilibrium was not seen for any samples, which they were for Shi et al. [14] at temperatures 1050 °C and above, however for lower strain rates.

This data agrees well with the tests performed by Shi, et al. [14]. With increasing strain rate the adiabatic heating increased which explains the large softening rate seen for samples deformed at  $5 \text{ s}^{-1}$ , figures 5.2 (c,f). Because dDRX is thermally driven, a higher temperature would increase the rate of dDRX as well as thermal softening, leading to a lower stress.

Figure 5.3 shows three different temperature evolutions with deformation. For the lowest strain rate, figure 5.3 (a,d) the slight increase in temperature from

adiabatic heating does not cause a severe increase in temperature and the heating system can stabilize it after a couple of seconds. For the intermediate strain rate, figure 5.3 (b,e), the heat generated during deformation is higher, so the response from the heating system will be more impactful, which led to the temperature getting below target at a strain of about 0.65, and continued to decrease until WQ was initialized. For  $5 \text{ s}^{-1}$ , figure 5.3 (c,f), the generated adiabatic heating was so high, the temperature continued to increase even though the Gleeble tried to compensate. Unfortunately, this is seldom reported in the literature. Instead, only the maximum temperature is plotted, as shown for this data in figure 5.4, in order to establish the adiabatic heating, or calculated temperature-curves neglecting heating system response are reported. However, as can be seen in figure 5.3 the temperature should be investigated throughout the whole deformation procedure, since different strain rates produce different responses, and there exist strain rates where the temperature will go below target, and not only be heated. Another thing that could be derived from this inspection was that the Gleeble was programmed based on time, so for when deforming at  $5 \text{ s}^{-1}$ , the heating did turn off before deformation was complete, due to the extra time needed for acceleration and deceleration. This is visible as the "jump" in temperature for one point, figure 5.3 (c,f). Showing the maximum measured temperature, figure 5.4, does give some useful information. Adiabatic heating increases with strain rate, while the increase gets lower, compared to the target temperature, with increasing compression temperature. As can be seen from figure 5.4, samples deformed at  $1080 \text{ }^\circ\text{C}$ ,  $5 \text{ s}^{-1}$  actually were heated above the carbide solvus, but only for

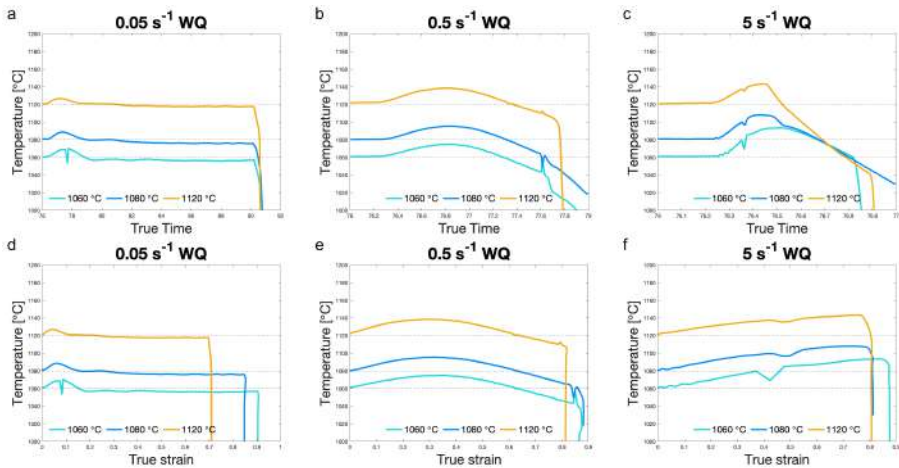


Figure 5.3: Temperature evolution during deformation for each strain rate based on a) - c) time and d) - f) true strain. Horizontal lines show the target temperatures.

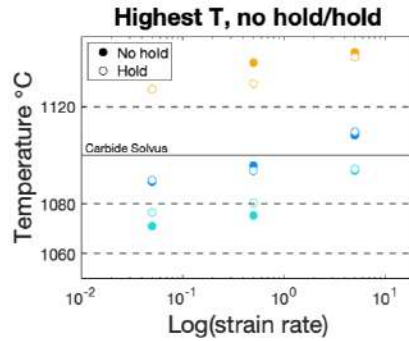


Figure 5.4: The highest measured temperature for each sample either quenched (filled circles) or held prior to quenching (empty circles). The dashed lines show the three target temperatures while the solid line show the carbide solvus temperature.

a fraction of a second which should not contribute to any dissolution of grain boundary carbides.

## 5.2.2 Recrystallization

IPF maps of the microstructure acquired from the centre of the Gleeble sample volume is shown in figure 5.5. The area is  $500 \times 500 \mu\text{m}$ . Deformation at supersolvus  $1120 \text{ }^\circ\text{C}$ , figure 5.5 (g-i), yielded a microstructure with larger recrystallized grains and fewer remaining deformed ones compared to deformation at sub-solvus, figure 5.5 (a-f). Another observation is that deformation at  $1120 \text{ }^\circ\text{C}$  also yielded similar microstructures for all three strain rates. Deformation at sub-solvus temperatures, on the other hand, resulted in microstructure more affected by strain rate, where deformation at the intermediate strain rate, figure 5.5 (b,e) showed much smaller grains compared to the other strain rates.

This is further showed in figure 5.6 where grain size distributions of recrystallized grains for each sample quenched directly after deformation is shown in figure 5.6 (a-c) for each strain rate respectively. Note that grain diameters are presented on a  $\log_{10}$ -scale in order to better visualize the distributions of the smaller grains present in  $1060 \text{ }^\circ\text{C}$  and  $1080 \text{ }^\circ\text{C}$  in figure 5.6 (b). Increased deformation temperature present led to larger grains visible in histograms, figure 5.6 (a-c) as well as in 5.6 (d), which shows the average grain diameter and standard deviation for recrystallized grains. Comparing the sub-solvus temperatures ( $1060 \text{ }^\circ\text{C}$  and  $1080 \text{ }^\circ\text{C}$ ) for each strain rate in figure 5.6 (d) the average grain size and standard deviation are very similar for samples deformed at these

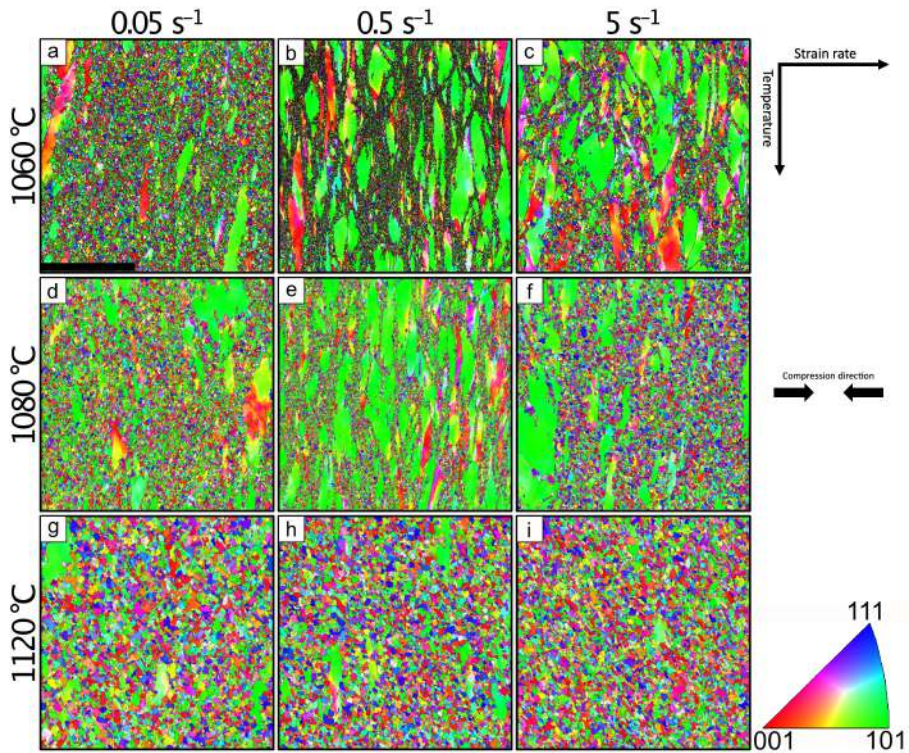


Figure 5.5: IPF maps over samples WQ directly after deformation. Acquired from the centre of each deformed sample. Increasing strain rate from left to right and increasing temperature from top to bottom. Legend in bottom right corner gives information on crystallographic orientation, parallel to compression axis, and colour. Scale bar is 200  $\mu\text{m}$ .

temperatures at the lowest strain rate  $0.05 \text{ s}^{-1}$ . With increasing strain rate, the average grain size increased for samples compressed at  $1080 \text{ }^\circ\text{C}$  compared to  $1060 \text{ }^\circ\text{C}$ , which is attributed to the higher adiabatic heating. The lowest average diameter was measured during compression at  $0.5 \text{ s}^{-1}$  for both temperatures. For  $0.5$  and  $5 \text{ s}^{-1}$ , grain growth mainly occurs during mDRX at the quench delay (due to the fast deformation rates). Because the temperature is lower at this stage for the strain rate  $0.5 \text{ s}^{-1}$  the grain growth is not as efficient. At the lowest strain rate,  $0.05 \text{ s}^{-1}$ , the deformation time is so long that grains should have time to grown even during deformation, this together with the temperature stabilizing quickly, figure 5.3 (a,d), suggests that purely deformation temperature does not lead to significant changes in microstructure between  $1060 \text{ }^\circ\text{C}$  and  $1080 \text{ }^\circ\text{C}$ . Deformation at  $1120 \text{ }^\circ\text{C}$  show that the response from the adiabatic heating is not as impactful as when deforming at lower temperatures. The average grain size and spread was very similar for  $1120 \text{ }^\circ\text{C}$ ,

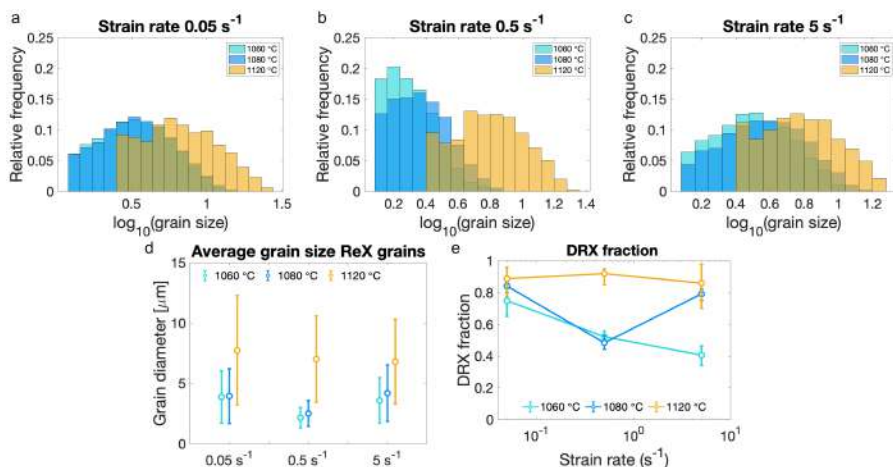


Figure 5.6: Grain size statistics over samples WQ directly after deformation. (a - c): grain size distribution over recrystallized grains, where (a) show deformation with strain rate  $0.05 \text{ s}^{-1}$ , (b)  $0.5 \text{ s}^{-1}$  and (c)  $5 \text{ s}^{-1}$ . (d) show recrystallized fraction for each sample, and (e) average grain size with standard deviation.

$0.5$  and  $5 \text{ s}^{-1}$ . However, the longer deformation time during  $0.05 \text{ s}^{-1}$  seemed to have led to an increased grain growth.

For a quantitative analysis, recrystallized vs deformed grains were separated based on a equivalent diameter cut off size, specific for each sample. These cut off diameters, for samples quenched directly after deformation, are presented in table 5.1. The DRX fractions for each sample are presented in figure 5.6 (e). The upper and lower limits of the error bars presented indicate the DRX fraction of the DRX cut off grain diameter was set to 1.5 and 0.8 of the set cut off diameter. The DRX fraction decreased with increasing strain rate for samples deformed at  $1060 \text{ }^\circ\text{C}$ , while deformation at  $1080 \text{ }^\circ\text{C}$  showed a "v"-shaped behaviour with the lowest DRX fraction occurring after deformation at  $0.5 \text{ s}^{-1}$  and higher for both  $0.05 \text{ s}^{-1}$  and  $5 \text{ s}^{-1}$ . As mentioned by Nicolay et al. [76], this "v"-shape is often referred to as the critical strain rate, above which

Table 5.1: Equivalent grain diameter cut off sizes determining if the grain is recrystallized or deformed .

Subset	Strain rate		
	$0.05 \text{ s}^{-1}$	$0.5 \text{ s}^{-1}$	$5 \text{ s}^{-1}$
Soak $1060 \text{ }^\circ\text{C}$ , def $1060 \text{ }^\circ\text{C}$	$12 \text{ }\mu\text{m}$	$7 \text{ }\mu\text{m}$	$10 \text{ }\mu\text{m}$
Soak $1080 \text{ }^\circ\text{C}$ , def $1080 \text{ }^\circ\text{C}$	$15 \text{ }\mu\text{m}$	$7 \text{ }\mu\text{m}$	$15 \text{ }\mu\text{m}$
Soak $1120 \text{ }^\circ\text{C}$ , def $1120 \text{ }^\circ\text{C}$	$25 \text{ }\mu\text{m}$	$21 \text{ }\mu\text{m}$	$18 \text{ }\mu\text{m}$

the dDRX is said to be accelerated. Nicolay et al. [76], however, claim that it is pDRX during the quench delay, and not the dDRX, that is accelerated due to the higher adiabatic heating. With increase in strain rate the deformation time decreases while the quench delay remains constant, leading to the fraction of time the microstructure undergoes dDRX compared to pDRX decreases. Deformation at 1120 °C, showed both the highest DRX fraction of the investigated temperatures at all three strain rates, and showed practically the same DRX fraction for all strain rates.

The temperature effect on dDRX is also shown by Shi et al. [14] who investigated Haynes 282. Increasing temperature led to both increase in recrystallized fraction and grain size, attributed to the higher diffusion rate at higher temperatures, which increased the HAGB mobility of recrystallized grains. Shi et al. also reported the lowest DRX progress at a strain rate of  $1 \text{ s}^{-1}$  which could possibly also be explained by the response of the Gleeble. Their study did not show the temperature evolution during deformation, so a clear correlation cannot be drawn that the similar responses are due to the Gleeble.

Gardner et al. [15] did both single, and multipass compression tests of Haynes 282, all at a temperature of 1100 °C, and their stress-strain data for the single pass test showed flow softening, reaching steady state flow at a strain of 0.8 during deformation with a strain rate of  $0.2 \text{ s}^{-1}$ . It should be noted that their tests were performed in a hydraulic deformation rig with a furnace, making the temperature much more stable during deformation since the heating was not controlled based on the samples temperature. Gardner et al. [15] also saw complete recrystallization of their microstructures. However, they cooled their samples through air cooling. Most likely, mDRX occurred here, consuming the deformed grains present right after deformation.

The primary mode of recrystallization for all investigated parameters is deemed to be dDRX. A clear necklace structure, a result of new grains nucleating at grain boundaries of deformed grains. This is also a reasonable assumption since Haynes 282 has a relatively low stacking fault energy, being estimated to  $\sim 28 \text{ mJm}^{-2}$  by Polkowska et al. [77].

Figure 5.7 show grain boundary serrations/bulging indicated by black arrows in figure 5.7 (a,b), which indicates that the strains inside deformed grains are localized and that it is this localization of strain that drives nucleation, and not the overall stored energy. In the upper section, the left grain bulges into the right and vice versa in the lower section. The white arrows in figure 5.7 (b,e) show two regions with a localized high strain in deformed grains. The white rectangles in figure ?? (a,b) show nucleation through the evolution of a subgrain structure, which is analogous to how cDRX operate. However, cDRX usually occurs uniformly throughout an entire grain, and not just at the grain boundaries [38], and at larger strains than investigated here. It has, however,

been suggested that the initial stages cDRX can be similar to dDRX, [78], and therefore occur in low  $\gamma_{SFE}$  materials as well, though localized to grain boundaries. Nucleation by twinning was also observed. White rectangles in figure 5.7 (c-e), more specifically marked with black arrows in 5.7 (d), show nucleated grains that have been cut off from their parent grain by a  $\Sigma 3$  boundary.

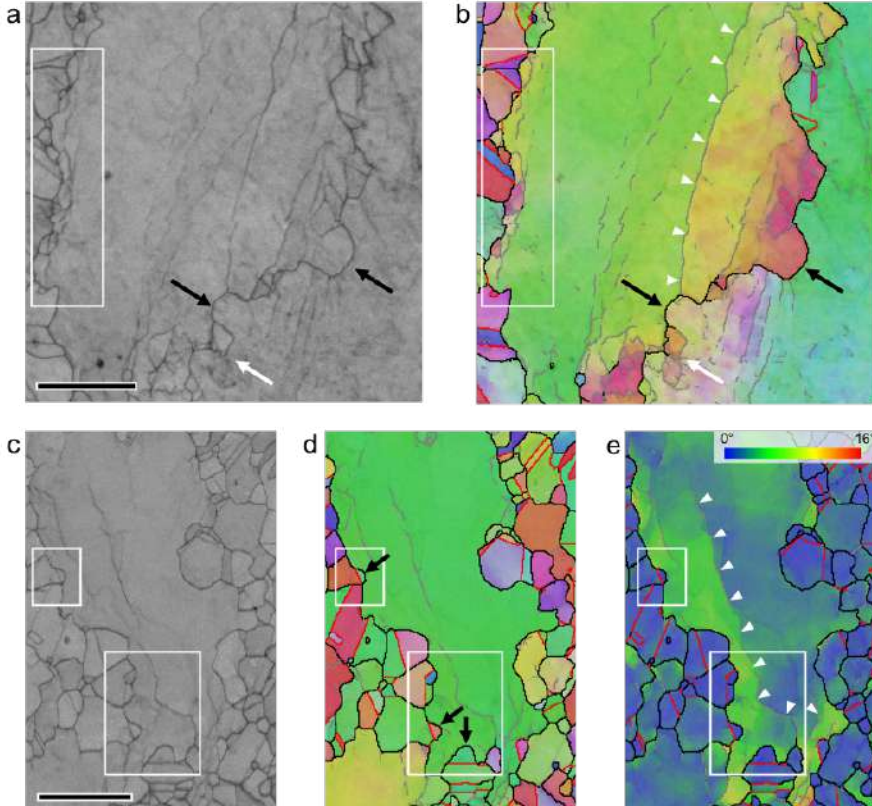


Figure 5.7: Nucleation phenomena occurring at grain boundaries of deformed grains for the sample deformed at 1080 °C, 0.05 s<sup>-1</sup>. (a, b) show the band contrast and IPF map of a region where nucleation occurs by serration/bulging of grain boundaries (black arrows), and subgrain rotations (white rectangle and white arrow). (c - e) show band contrast, IPF and GROD map respectively of another region. Here nucleation occurs by a grain nucleating by being cut off with a twin (black arrows). Two long misorientation fronts seen as a LAGB are marked by white arrow heads in (b, e). Scale bar is 20  $\mu\text{m}$ .

Nucleation through PSN was also seen to occur frequently in Haynes 282 for the deformation procedures investigated. Only MC particles were large and stable enough during material flow to accumulate the necessary  $\rho_d$  needed to drive

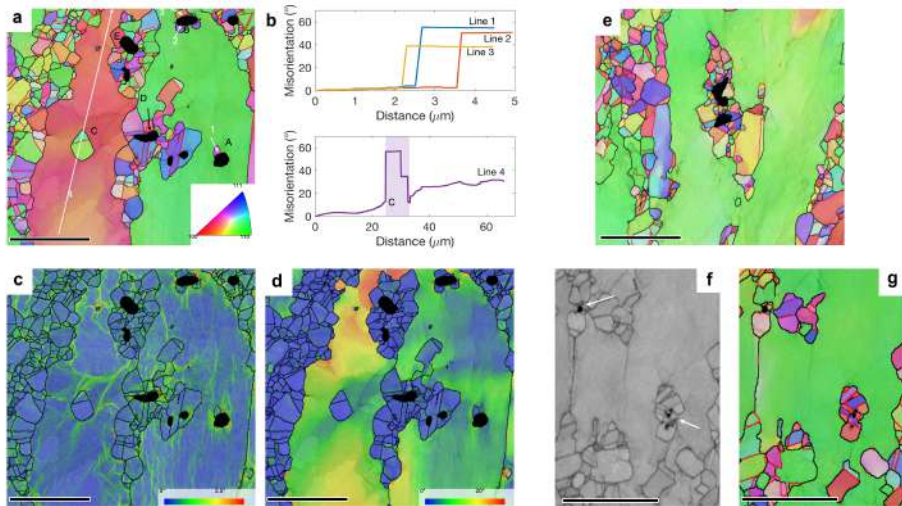


Figure 5.8: IPF maps with carbides marked in black. Clear nucleation and growth has occurred intragranually with carbides as nucleation sites.

nucleation. What differed PSN from dDRX and cDRX at grain boundaries was that there was no clear "inheritance" of the  $\{110\}$  parallel deformation direction, and no texture preference was observed. Figure 5.8 (b) shows the misorientation profiles between grains marked 1-4 in figure 5.8 (a) with the lowest misorientation being almost  $40^\circ$ . The grains marked "C" in figure 5.8 (a) has likely nucleated through PSN with a carbide either above or below the plane investigated. Figure 5.8 (c,d) show the KAM and GROD maps respectively showing the high local strains around the MC carbides.

### 5.3 Effect of secondary grain boundary carbides

During the initial 30 min soak at sub-solvus carbide temperatures ( $1060^\circ\text{C}$ ,  $1080^\circ\text{C}$ ), carbides nucleated and grew at the grain boundaries, as is shown in figure 5.9. Black arrows in figure 5.9 (b), and white arrows in 5.9 (c) show small round carbides on a random HAGB. It has been shown that  $\text{M}_{23}\text{C}_6$  carbides have different morphologies based on the interfacial energy [17], and in a random HAGB they form with an orientation similar to one of the grains, and continue to grow into the other grain. However, neither ECCI nor SE give information of the misorientation angle like EBSD, and a correlation has not been made to establish the angles for these boundaries. Gray and black arrows in figure 5.9 (c) show smaller carbides on a incoherent  $\Sigma 3$  boundary and no carbides on a coherent  $\Sigma 3$  boundary due to their low interfacial energy.

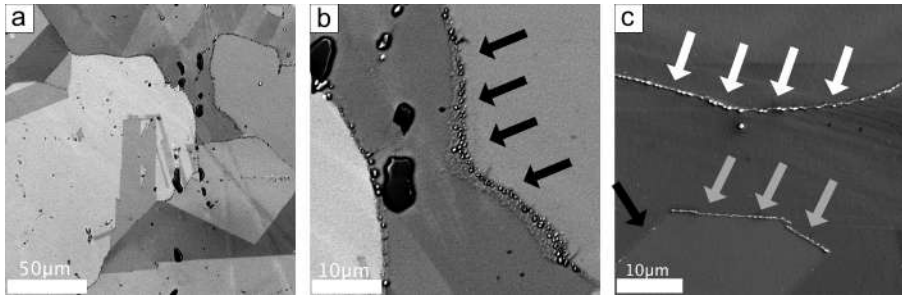


Figure 5.9: Grain boundary carbides morphology existing in Haynes 282 that has been soaked at 1080 °C for 30 minutes with a subsequent WQ. (a) and (b) are ECCI images also capturing difference in grain orientation. (c) is a SE image showing different morphologies of carbides for different HAGB.

The true stress-strain curves comparing samples deformed at 1080 °C with and without carbides are shown in figure 5.10 (a). A lower flow stress was measured for all samples without grain boundary carbides, however, inspecting the temperature for these samples showed that this was higher for each sample without carbides as well, figure 5.10 (b). The higher temperatures measured for samples without grain boundary carbides are more likely caused by experimental factors than a difference in the material properties caused by carbides. Figure 5.10 (c) shows a linear increase in temperature, during the last seconds of the pre deformation hold, for the sample without grain boundary carbide while it is maintained stable for the sample with. Figure 5.10 (c) only shows the samples deformed at  $0.5 \text{ s}^{-1}$ , but similar observations were made for the other strain rates as well, and are largely responsible for the apparent higher adiabatic heating in samples without grain boundary carbides.

The increase in stress at a strain of around 0.7 for the sample deformed at  $0.5 \text{ s}^{-1}$  without grain boundary carbides, seen in figure 5.10 (a), was caused by the thermocouple disconnecting, which led to even further cooling. An approximation of this cooling was made and is presented in in figure 5.11. Here, the power angle and temperature are plotted vs time. During the quench delay, the cooling rate was assumed to be linear, indicated by the solid black line. This rate was extrapolated from the point where the thermocouple was disconnected, dashed green line, to where the Gleeble should have turned off the heating, and the approximate temperature difference between the samples caused the thermocouple disconnection was  $\sim 10 \text{ }^\circ\text{C}$  (horizontal dashed lines). This gives an upper bound, on the approximated drop in temperature, and the real difference was probably lower, due to the adiabatic heating that still occurred since deformation was ongoing. This should have led to a lower cooling rate then during quench delay, where no adiabatic heating occurs.

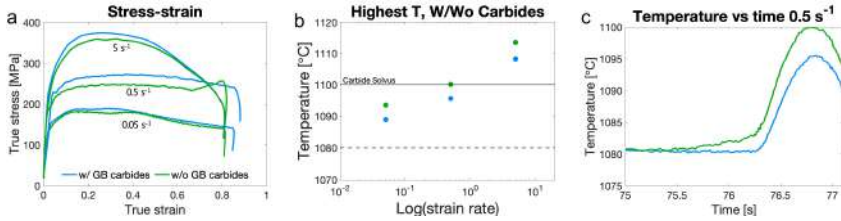


Figure 5.10: (a) true stress-strain curves for samples with grain boundary carbides (blue) and without grain boundary carbides (green) for all three strain rates. (b) highest measured temperature from adiabatic heating. (c) irregularities observed in the Gleeble data during temperature stabilization.

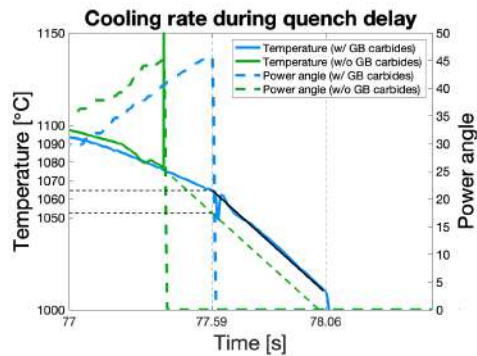


Figure 5.11: Approximation of cooling for  $1080 \text{ °C}$   $0.5 \text{ s}^{-1}$  with no grain boundary carbides.

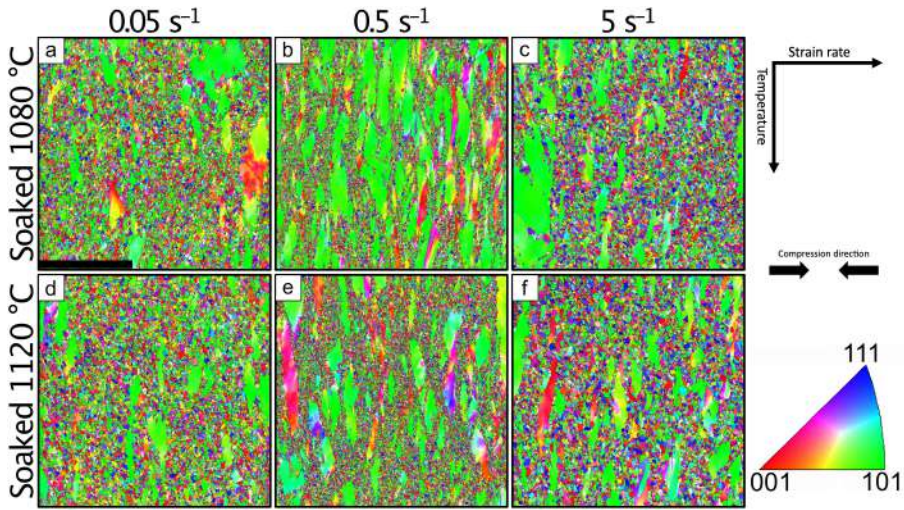


Figure 5.12: IPF maps over samples deformed at 1080 °C with (top row) and without (bottom row) grain boundary carbides. Acquired from the centre of each deformed sample. Increasing strain rate from left to right. Legend in bottom right corner gives information on crystallographic orientation and colour. Scale bar is 200  $\mu\text{m}$ .

A comparison of microstructures are shown in the IPF maps in figure 5.12 with samples that contained grain boundary carbides during compression are shown figure 5.12 (a-c) and samples without grain boundary carbides are shown in 5.12 (d-f). The area for each map is  $500 \times 500 \mu\text{m}$ . Any indication that the presence of carbides affect the resulting microstructure was not seen.

This is further shown in figure 5.13 (a-d), where grain size distributions in the recrystallized fractions (defined by cut-off grain sizes given in table 5.2) appear practically identical for samples deformed at each strain rate both with and without carbides. Samples deformed without carbides show a marginal shift to a distribution of larger grains. However, since the shift was small and the temperature of the samples without carbides were slightly higher during deformation, as preciously described, the difference cannot be conclusively assigned to a material response.

One thing to note here is that even though the rate of mDRX is temperature dependent, the assumed 10 °C difference between samples deformed at  $0.5 \text{ s}^{-1}$  due to the disconnection of the thermocouple, their grain distributions are still very similar, and looking at the recrystallized fraction, figure 5.13 (e), the sample with the disconnected thermocouple shows a higher fraction, even outside the margin of error. This is further explained in article 2, but

Table 5.2: Equivalent grain diameter cut off sizes determining if the grain is recrystallized or deformed.

Subset	Strain rate		
	$0.05 \text{ s}^{-1}$	$0.5 \text{ s}^{-1}$	$5 \text{ s}^{-1}$
Soak $1080 \text{ }^\circ\text{C}$ , def $1080 \text{ }^\circ\text{C}$	$15 \text{ }\mu\text{m}$	$7 \text{ }\mu\text{m}$	$15 \text{ }\mu\text{m}$
Soak $1120 \text{ }^\circ\text{C}$ , def $1080 \text{ }^\circ\text{C}$	$18 \text{ }\mu\text{m}$	$8 \text{ }\mu\text{m}$	$15 \text{ }\mu\text{m}$

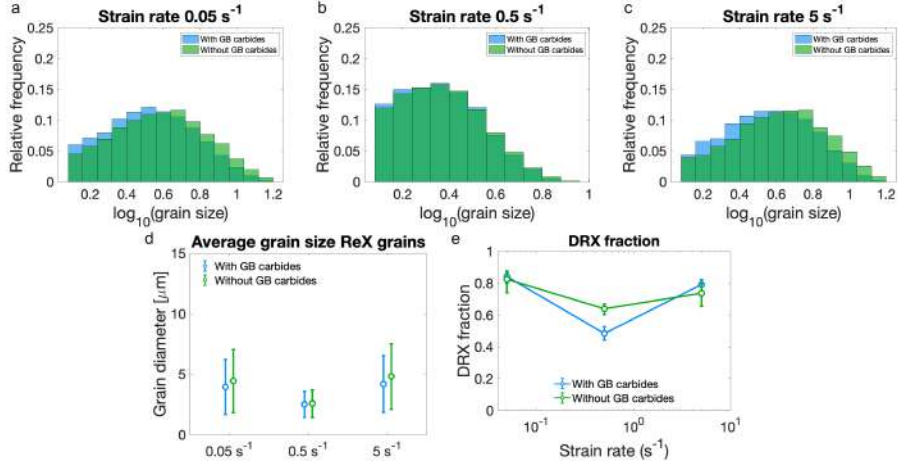


Figure 5.13: Comparison of grain statistics for recrystallized deformed at  $1080 \text{ }^\circ\text{C}$  with, or without grain boundary carbides, where (a - c) show grain size distributions after deformation with strain rate of (a)  $0.05 \text{ s}^{-1}$ , (b)  $0.5 \text{ s}^{-1}$  and (c)  $5 \text{ s}^{-1}$ . (d) show the average grain size with standard deviation and (e) recrystallized fractions for each sample.

a reason for this could be different durations of the quench delay, which has been measured to differ between  $0.5 - 2 \text{ s}$  for different samples. It is, however, impossible to compare the quench delays for the samples deformed at  $0.5 \text{ s}^{-1}$  due to the lack of a recorded sample temperature beyond the point of where the thermocouple disconnected.

Figure 5.14 shows ECCI images of different areas of a compressed sample, that has been etched in order to reveal the carbides. Figure 5.14 (a,b) were acquired from areas contained in the IPF map shown in figure 5.12 (a) while figure 5.14 (c,d) show areas closer to the sample edges, where the strain was less and the area is not as recrystallized. The white ovals in figure 5.14 (a,b) contains lines of grain boundary carbides that now lie both intra- and intergranally through the recrystallized grains, presumably in lines that were grain boundaries prior to deformation. Arrows in figure 5.14 (b) show a boundary between a deformed grain (left) and recrystallized region (right), with no visible carbides along it.

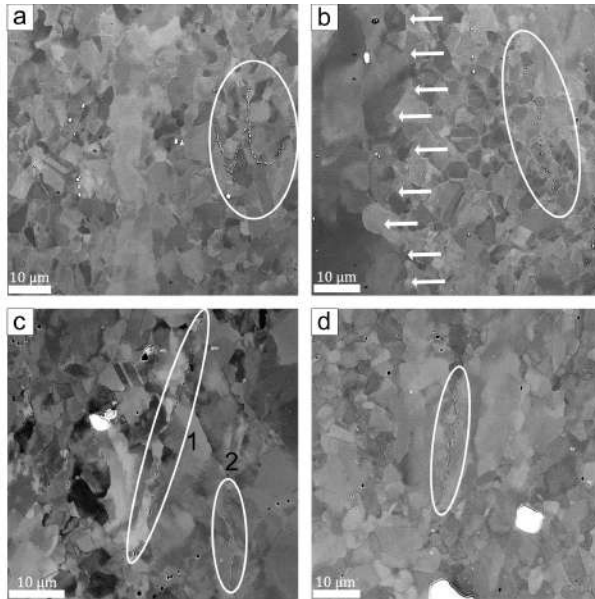


Figure 5.14: ECCI images captured from the sample deformed at 1080 °C,  $0.05 \text{ s}^{-1}$  with grain boundary carbides present marked with red ovals. (a, b) are from the centre of the sample while (c, d) are in regions closer to the edge.

Going further out, figure 5.14 (c,d) grain boundary carbides are present at grain boundaries, oval 1 and 2 in (c) while the oval in (d) shows a grain boundary where no carbides are seen. One thing to note is that the amount of carbides seem a lot less than for the non compressed, soaked pieces, figure 5.9. The reason for this is unknown. Deformation at  $0.05 \text{ s}^{-1}$  should not have raised the temperature to 1100 °C, so carbide dissolution should be caused by something else, either the applied strain, or due to DRX.

The concluding remark in regards to the role of grain boundary carbides during deformation at sub-solvus temperatures is that no mechanical or microstructural differences observed could be deduced to occur by changes in material properties, and are instead attributed to experimental variations. So if the carbides have any effect, it is insignificant and other parameters like temperature should instead be taken into consideration when deforming Haynes 282 below the carbide solvus temperature.

## 5.4 Effect of post dynamic recrystallization

Since industrial pieces are not, or cannot be, quenched quickly due to size or risk of cracking. Instead, they are air cooled and will maintain a high temperature for a time after deformation. It is therefore important to study pDRX that will occur during this time since recrystallization will continue post deformation. As mentioned in chapter 3, the terminology of post dynamic recrystallization can vary. However, since the microstructure contains a large fraction of recrystallized grains after deformation, figure 5.5, and the holding time is only 90 s, the probability that dSRX (i.e. nucleation and growth of new grains) is low, and the pDRX process is fully attributed to grain growth of already nucleated grains through mDRX [79].

During the 90 s hold the grain growth was rather evident, and the microstructure is deemed fully recrystallized for all temperatures and strain rates, figure 5.15. The effect of the strain rate seen for dDRX has disappeared. Looking at the grain size distributions presented for the hold samples in figure 5.16 (a-c), and average grain sizes, figure 5.16 (d), shows that only temperature seem to affect the resulting microstructure, with grain sizes increased with increasing temperature. This has also been shown by Metzler et al. [80], who showed that total strain did not matter for the inspected strains (0.4 and 0.82). They investigated temperatures 1100 °C, 1150 °C and 1200 °C, and saw a larger average grain size after a 60 s hold for 1150 °C and 1200 °C than was seen here after 90 s at 1120 °C. They also found that the calculated velocity of grain growth was higher than expected, suggesting that residual stored energy can contribute to an acceleration in grain growth at the initial stages, where deformed grains, are still present. Nicolay et al. [64, 76] showed that with good enough angular resolution, it is possible to distinguish between grains that have recrystallized during dDRX and those that have done so after deformation. dDRX grains that grow while compression is still ongoing will also be strained, while nuclei that grow during a static hold will not, making it possible to distinguish them. However, with the angular resolution of the data in this work, this is not possible.

The microstructure became textured with a fibre  $\langle 110 \rangle$  texture parallel to the deformation direction during compression. This can be seen in figure 5.17 which shows the textures for deformed and DRX grains from the samples WQ directly after deformation, as well as the texture of the complete microstructure for samples held at the deformation temperature for 90 s prior to WQ. The texture from the deformed grains, seen in the left most columns for each temperature in figure 5.17, was adopted by the DRX grains, middle column. This effect was less pronounced with increasing strain rate where texture is more random for samples deformed at  $5 \text{ s}^{-1}$ . However, it is also weaker in samples deformed at 1120 °C, suggesting this may be temperature dependent, and the

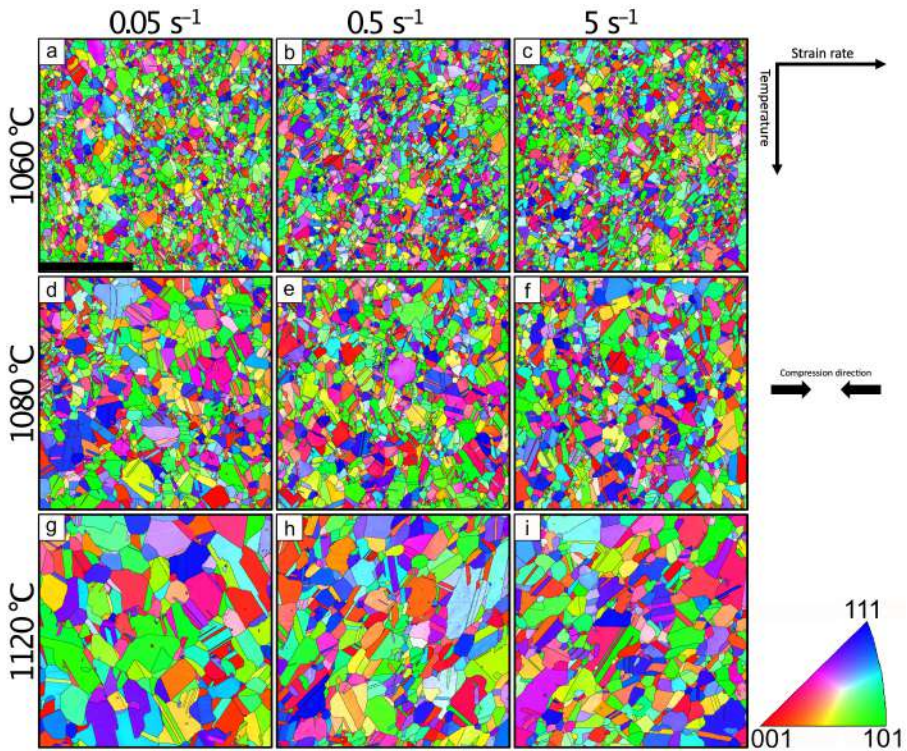


Figure 5.15: IPF maps over samples held for 90 s prior to WQ. Acquired from the centre of each deformed sample. Increasing strain rate from left to right and increasing temperature from top to bottom. Legend in bottom right corner gives information on crystallographic orientation and colour. Scale bar is 200  $\mu\text{m}$ .

increase in temperature from the adiabatic heating at  $5 \text{ s}^{-1}$  is what causes this weakening for 1060 and 1080 °C. The  $\langle 110 \rangle$  texture parallel to the deformation direction is not as clear in the deformed grains for samples deformed at 1120 °C most likely to the very low statistics. Comparing with figure 5.5, lowest row, the microstructures are almost completely recrystallized.

The texture became randomized during the 90 s hold, figure 5.17, and could be seen as completely random for 1080 °C and 1120 °C while sampled held at 1060 °C still showed some texture, though weaker than the recrystallized grains after deformation. This was attributed to the generation and growth of annealing twins that occurred during mDRX. The  $\Sigma 3$  boundaries create  $60^\circ$  misorientation between the parent and twin. This is further portrayed in figure 5.18 showing the  $\Sigma 3$  boundary fractions for samples held at 90 s prior to WQ. Figure 5.18 show the fraction of  $\Sigma 3$  boundaries as steps for certain

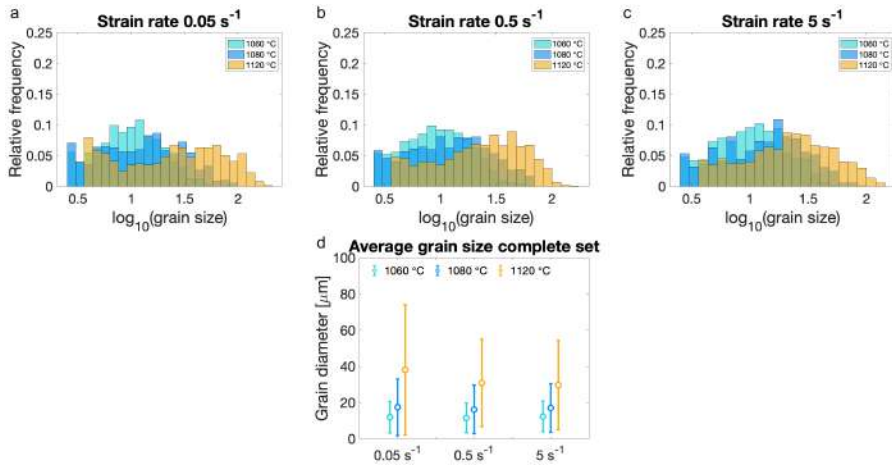


Figure 5.16: Comparison of grain statistics for grains from samples held for 90 s prior to WQ. (a - c) show grain size distributions after deformation and hold with strain rate of (a)  $0.05 \text{ s}^{-1}$ , (b)  $0.5 \text{ s}^{-1}$  and (c)  $5 \text{ s}^{-1}$ . (d) shows the average grain size with standard deviation for each sample.

grain size intervals. Due to statistics, the intervals get larger with increase in grain size, and each fraction is the average for that interval.

With increasing grain size, the  $\Sigma 3$  boundary fraction increases since the boundaries grow with the grains. New twins can also be created with grain growth due to stacking faults [49]. The twin boundary fraction was also seen to increase with temperature, being higher in samples deformed at 1080 °C and 1120 °C, also showing a steeper increase compared to 1060 °C. The randomization of the inherited texture on the recently recrystallized grains seen in figure 5.17 is attributed to the increase in  $\Sigma 3$  boundaries with grain growth during the post deformation hold.

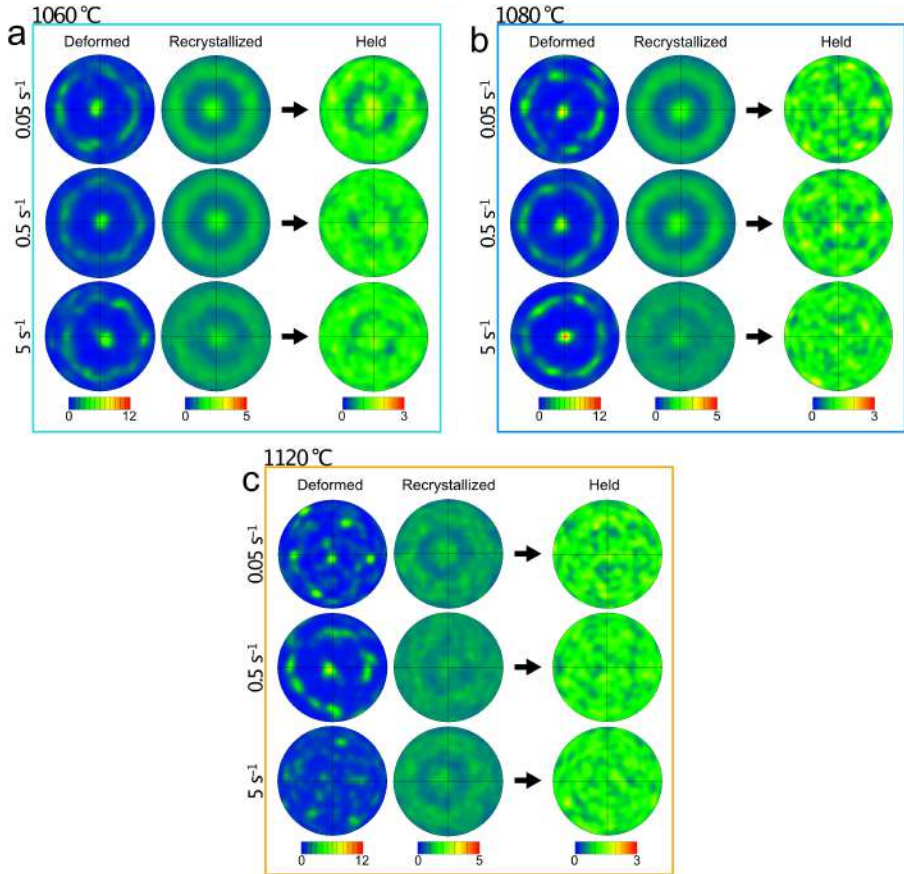


Figure 5.17: Texture evolution of Haynes 282 during deformation and post deformation hold. (a) show pole figures in the  $\langle 110 \rangle$  direction for deformed and recrystallized grains in samples WQ directly after deformation, and all grains for the held samples. (b) show these pole figures for samples deformed at 1080 °C and (c) for samples deformed at 1120 °C.

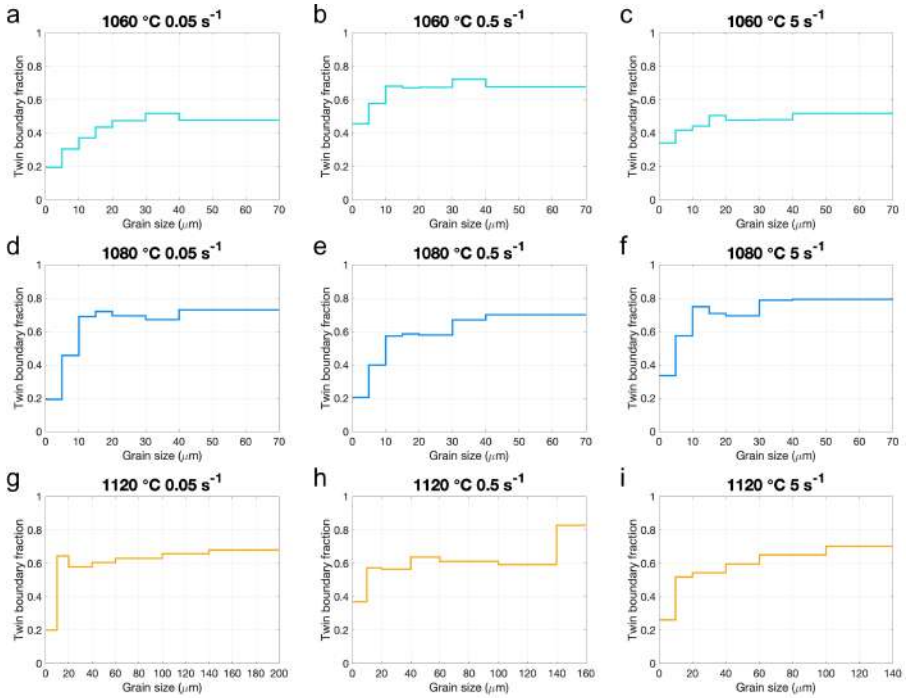


Figure 5.18: Twin boundary fraction with increasing grain size. (a - c) show stair graphs for the  $\Sigma 3$  fractions for  $0.05 \text{ s}^{-1}$ ,  $0.5 \text{ s}^{-1}$  and  $5 \text{ s}^{-1}$  respectively. (d - f) for 1080 °C samples and (g - i) for 1120 °C samples. Please note that values on the x-axis are not uniform since grains in 1120 °C samples were a lot larger.

## CHAPTER 6

---

### Future research

---

The work done has been in order to answer how deformation at subsolvus temperatures affects the recrystallization and final microstructure, if the presence of secondary grain boundary carbides have any effect and how a post deformation hold will evolve the microstructure through post dynamic recrystallization.

It was found that recrystallization progressed through a clear nucleation, and subsequent growth, indicating dDRX. Nucleation mainly occurred at grain boundaries that, during deformation, became serrated due to localized strains in grains. PSN on primary MC carbides was also evident, and was caused by accumulation of dislocations at MC carbides. Recrystallization at grain boundaries adopted the texture of the deformed grains while no texture could be seen at PSN nucleated grains. However, during the 90 s hold, the effects of strain rate were erased and only temperature affected the resulting microstructure. The presence of secondary carbides at grain boundaries did not seem to contribute any changes to the recrystallization, meaning that when hot compression at sub solvus temperatures is performed, the temperature is the main factor to consider.

This work has given answers to the first milestone of the project, the forging process, where the microstructure was changed through dynamic and

post-dynamic recrystallization. The next step in understanding the thermo-mechanical processing of Haynes 282 will be to perform heat treatments on the hot deformed samples. In order to gain understanding of most interest for industry, only samples that were statically held for 90 s before being WQ will be subjected to heat treatments. Industrial applications air cool the forged pieces, so mDRX is always occurring, making microstructures after a 90 s holding more similar to industrial pieces. These heat treatments will nucleate and grow the strengthening precipitates like  $\gamma'$  intragranularly and GB carbides at the new grain boundaries. New microstructural analysis through 3D-EBSD at grain to evaluate grain growth and evolution of HAGB and CSL boundaries. Characterization and analysis of the strengthening phases will be evaluated with electron microscopy. Heat treatments will follow the procedure shown in figure 2.3.

It should also be noted that recrystallization happens in 3-D, while all results have been given in 2-D cross sections. Another step to further gain understanding of recrystallization will be 3-D EBSD, with a start at PSN. Evaluating PSN around a MC carbide in all three dimensions could give a further insight into the phenomena. Inspecting twin boundaries with 3-D methods is also of interest since the misorientation they create in grains with grain growth affect the texture.

The third step is to evaluate the mechanical properties, mainly the creep resistance, resulting the thermomechanical processing. For industrial significance, the Gleeble samples are too small to do this testing on. Instead, full sized pancakes forgings will be used to allow extraction of mechanical test specimens with standardized geometry. The aim of this is to develop a thermomechanical procedure that yields the optimal mechanical properties, and the academic knowledge to understand, and explain, the change of mechanical properties with the evolution of the microstructure through forging and heat treatments.

---

## Bibliography

---

- [1] Roger C Reed. *The Superalloys : Fundamentals and Applications*. Cambridge University Press, Cambridge, UNITED KINGDOM, 2006.
- [2] Jeremy E Watson. *Superalloys : Production, Properties and Applications*. Nova Science Publishers, Incorporated, New York, UNITED STATES, 2011.
- [3] L M Pike. Development of a Fabricable Gamma Prime ( $\gamma$  prime) Strengthened Superalloy. In *Proceedings of the International Symposium on Superalloys*, pages 191–200, 2008.
- [4] Ceena Joseph, Christer Persson, and Magnus Hörnqvist Colliander. Influence of heat treatment on the microstructure and tensile properties of Ni-base superalloy Haynes 282. *Materials Science and Engineering: A*, 679:520–530, 2017.
- [5] Nitesh Raj Jaladurgam, Hongjia Li, Joe Kelleher, Christer Persson, Axel Steuwer, and Magnus Hörnqvist Colliander. Microstructure-dependent deformation behaviour of a low gamma prime volume fraction Ni-base superalloy studied by in-situ neutron diffraction. *Acta Materialia*, 183:182–195, 2020.
- [6] Shreya Mukherjee, Kaustav Barat, S Sivaprasad, Soumitra Tarafder, and Sujoy Kumar Kar. Elevated temperature low cycle fatigue behaviour of Haynes 282 and its correlation with microstructure – Effect of ageing conditions. *Materials Science and Engineering: A*, 762:138073, 2019.

- [7] Kyeong-Yong Shin, Jin-Hyeok Kim, Mathieu Terner, Byeong-Ook Kong, and Hyun-Uk Hong. Effects of heat treatment on the microstructure evolution and the high-temperature tensile properties of Haynes 282 superalloy. *Materials Science and Engineering: A*, 751:311–322, 2019.
- [8] K Barat, M Ghosh, S Sivaprasad, Sujoy Kumar Kar, and S Tarafder. High-Temperature Low-Cycle Fatigue Behavior in HAYNES 282: Influence of Initial Microstructure. *Metallurgical and Materials Transactions A*, 49(10):5211–5226, oct 2018.
- [9] P Zhang, Y Yuan, H Yin, Y Gu, J Wang, M Yang, G Yang, and X Song. Tensile Properties and Deformation Mechanisms of Haynes 282 at Various Temperatures. *Metallurgical and Materials Transactions A*, 49(5):1571–1578, 2018.
- [10] Adelajda Polkowska, Wojciech Polkowski, Małgorzata Warmuzek, Natalia Cieśła, Grzegorz Włoch, Dariusz Zasada, and Robert M Purgert. Microstructure and Hardness Evolution in Haynes 282 Nickel-Based Superalloy During Multi-variant Aging Heat Treatment. *Journal of Materials Engineering and Performance*, 28(7):3844–3851, 2019.
- [11] Sylvio Haas, Joel Andersson, Martin Fisk, Jun-Sang Park, and Ulrich Lienert. Correlation of precipitate evolution with Vickers hardness in Haynes® 282® superalloy: In-situ high-energy SAXS/WAXS investigation. *Materials Science and Engineering: A*, 711:250–258, 2018.
- [12] Fabian Hanning, Abdul K Khan, Joachim Steffenburg-Nordenström, Olanrewaju Ojo, and Joel Andersson. Investigation of the Effect of Short Exposure in the Temperature Range of 750–950 °C on the Ductility of Haynes® 282® by Advanced Microstructural Characterization, 2019.
- [13] K A Rozman, G R Holcomb, C S Carney, Ö N Doğan, J J Kruzic, and J A Hawk. Effect of 730 °C Supercritical Fluid Exposure on the Fatigue Threshold of Ni-Based Superalloy Haynes 282. *Journal of Materials Engineering and Performance*, 28(7):4335–4347, 2019.
- [14] Zhaoxia Shi, Xiaofeng Yan, Chunhua Duan, Cunjiang Tang, and Enxiang Pu. Characterization of the Hot Deformation Behavior of a Newly Developed Nickel-Based Superalloy. *Journal of Materials Engineering and Performance*, 27(4):1763–1776, 2018.
- [15] S Gardner, W Li, M Coleman, and R Johnston. The effects of thermo-mechanical history on the microstructure of a nickel-base superalloy during forging. *Materials Science and Engineering: A*, 668:263–270, 2016.
- [16] Chester Thomas Sims, Norman F Stoloff, and William C Hagel. *Superalloys II*. Wiley, [revision] edition, 1987.

- [17] Rui Hu, Guanghai Bai, Jinshan Li, Jingqing Zhang, Tiebang Zhang, and Hengzhi Fu. Precipitation behavior of grain boundary M23C6 and its effect on tensile properties of Ni–Cr–W based superalloy. *Materials Science and Engineering: A*, 548:83–88, 2012.
- [18] Juraj Belan. GCP and TCP Phases Presented in Nickel-base Superalloys. *Materials Today: Proceedings*, 3(4):936–941, 2016.
- [19] L Liu, F Sommer, and H Z Fu. Effect of solidification conditions on MC carbides in a nickel-base superalloy IN 738 LC. *Scripta Metallurgica et Materialia*, 30(5):587–591, 1994.
- [20] Y C Lin, Jiao Deng, Yu-Qiang Jiang, Dong-Xu Wen, and Guan Liu. Hot tensile deformation behaviors and fracture characteristics of a typical Ni-based superalloy. *Materials & Design*, 55:949–957, 2014.
- [21] Pilar De Tiedra, Óscar Martín, and Manuel San-Juan. Potentiodynamic study of the influence of gamma prime and eta phases on pitting corrosion of A286 superalloy. *Journal of Alloys and Compounds*, 673:231–236, 2016.
- [22] J C. Zhao, V Ravikumar, and A M Beltran. Phase precipitation and phase stability in nimonic 263. *Metallurgical and Materials Transactions A*, 32(6):1271–1282, 2001.
- [23] S M Seo, I S Kim, J H Lee, C Y Jo, H Miyahara, and K Ogi. Eta Phase and Boride Formation in Directionally Solidified Ni-Base Superalloy IN792 + Hf. *Metallurgical and Materials Transactions A*, 38(4):883–893, 2007.
- [24] Bilal Hassan and Jonathan Corney. Grain boundary precipitation in Inconel 718 and ATI 718Plus. *Materials Science and Technology*, 33(16):1879–1889, nov 2017.
- [25] Matthew J Wong, Paul G Sanders, John P Shingledecker, and Calvin L White. Design of an Eta-Phase Precipitation-Hardenable Nickel-Based Alloy with the Potential for Improved Creep Strength Above 1023 K (750 °C). *Metallurgical and Materials Transactions A*, 46(7):2947–2955, 2015.
- [26] Emil Eriksson and Magnus Hörnqvist Colliander. Dynamic and Post-Dynamic Recrystallization of Haynes 282 below the Secondary Carbide Solvus, 2021.
- [27] Ceena Joseph. *Microstructure Evolution and Mechanical Properties of Haynes 282*. PhD thesis, Chalmers.
- [28] Ceena Joseph, Magnus Hörnqvist, and Christer Persson. Anisotropy of Room Temperature Ductility in Haynes®282® Forgings, nov 2014.

- [29] C Joseph, C Persson, and M Hörnqvist Colliander. Precipitation Kinetics and Morphology of Grain Boundary Carbides in Ni-Base Superalloy Haynes 282. *Metallurgical and Materials Transactions A*, 51(12):6136–6141, 2020.
- [30] C Joseph, M H Colliander, Rebecka Brommesson, and C Persson. Influence of carbide distribution on ductility of Haynes 282 forgings. 2016.
- [31] L O Osoba, A K Khan, and O A Ojo. Identification of Mo-based Precipitates in Haynes 282 Superalloy. *Metallurgical and Materials Transactions A*, 48(4):1540–1543, 2017.
- [32] Ruifeng Dong, Jinshan Li, Tiebang Zhang, Rui Hu, and Hongchao Kou. Elements segregation and phase precipitation behavior at grain boundary in a Ni-Cr-W based superalloy. *Materials Characterization*, 122:189–196, 2016.
- [33] H U Hong, B S Rho, and S W Nam. Correlation of the M<sub>23</sub>C<sub>6</sub> precipitation morphology with grain boundary characteristics in austenitic stainless steel. *Materials Science and Engineering: A*, 318(1):285–292, 2001.
- [34] Antariksh Rao Pratap Singh. *Mechanisms of ordered gamma prime precipitation in nickel base superalloys*. PhD thesis, Ann Arbor, 2011.
- [35] S L Semiatin, S-L. Kim, F Zhang, and J S Tiley. An Investigation of High-Temperature Precipitation in Powder-Metallurgy, Gamma/Gamma-Prime Nickel-Base Superalloys. *Metallurgical and Materials Transactions A*, 46(4):1715–1730, 2015.
- [36] Matthew J Donachie, S Donachie, Donachie Mj, and Donachie Sj. *Superalloys : A Technical Guide*. A S M International, Materials Park, UNITED STATES, 2002.
- [37] Taylan Altan, Gracious Ngaile, and Gangshu Shen. Cold and Hot Forging - Fundamentals and Applications.
- [38] K Huang and R E Logé. A review of dynamic recrystallization phenomena in metallic materials. *Materials & Design*, 111:548–574, 2016.
- [39] Taku Sakai, Andrey Belyakov, Rustam Kaibyshev, Hiromi Miura, and John J Jonas. Dynamic and post-dynamic recrystallization under hot, cold and severe plastic deformation conditions. *Progress in Materials Science*, 60:130–207, 2014.
- [40] N Dudova, A Belyakov, T Sakai, and R Kaibyshev. Dynamic recrystallization mechanisms operating in a Ni–20%Cr alloy under hot-to-warm working. *Acta Materialia*, 58(10):3624–3632, 2010.

- [41] Longfei Li, Wangyue Yang, and Zuqing Sun. Dynamic Recrystallization of Ferrite with Particle-Stimulated Nucleation in a Low-Carbon Steel. *Metallurgical and Materials Transactions A*, 44(5):2060–2069, 2013.
- [42] W Xu, M Ferry, J M Cairney, and F J Humphreys. Three-dimensional investigation of particle-stimulated nucleation in a nickel alloy. *Acta Materialia*, 55(15):5157–5167, 2007.
- [43] J D Robson, D T Henry, and B Davis. Particle effects on recrystallization in magnesium–manganese alloys: Particle-stimulated nucleation. *Acta Materialia*, 57(9):2739–2747, 2009.
- [44] M Hatherly, Anthony Rollett, F J Humphreys, and Gregory S Rohrer. *Recrystallization and Related Annealing Phenomena*. Elsevier Science & Technology, London, UNITED KINGDOM, 2004.
- [45] Jue Wang, Jian-Xin Dong, and Mai-Cang Zhang. Nucleation mechanisms of dynamic recrystallization for G3 alloy during hot compression. *Rare Metals*, 35, apr 2016.
- [46] R D Doherty, D A Hughes, F J Humphreys, J J Jonas, D.Juul Jensen, M E Kassner, W E King, T R McNelley, H J McQueen, and A D Rollett. Current issues in recrystallization: a review. *Materials Science and Engineering: A*, 238(2):219–274, 1997.
- [47] Xuefeng Tang, Baoyu Wang, Hongchao Ji, Xiaobin Fu, and Wenchao Xiao. Behavior and modeling of microstructure evolution during meta-dynamic recrystallization of a Ni-based superalloy. *Materials Science and Engineering: A*, 675:192–203, 2016.
- [48] Nathalie Bozzolo and Marc Bernacki. Viewpoint on the Formation and Evolution of Annealing Twins During Thermomechanical Processing of FCC Metals and Alloys. *Metallurgical and Materials Transactions A*, 51(6):2665–2684, 2020.
- [49] G Gottstein. Annealing texture development by multiple twinning in f.c.c. crystals. *Acta Metallurgica*, 32(7):1117–1138, 1984.
- [50] H Gleiter. The formation of annealing twins. *Acta Metallurgica*, 17(12):1421–1428, 1969.
- [51] M Frommert and G Gottstein. Mechanical behavior and microstructure evolution during steady-state dynamic recrystallization in the austenitic steel 800H. *Materials Science and Engineering: A*, 506(1):101–110, 2009.
- [52] Joshua McCarley, Randolph Helmink, Robert Goetz, and Sammy Tin. Grain Boundary Engineering of a Low Stacking Fault Energy Ni-based Superalloy. *Metallurgical and Materials Transactions A*, 48(4):1666–1677, 2017.

- [53] Joshua McCarley, B Alabbad, and S Tin. Influence of the Starting Microstructure on the Hot Deformation Behavior of a Low Stacking Fault Energy Ni-based Superalloy. *Metallurgical and Materials Transactions A*, 49(5):1615–1630, 2018.
- [54] S S Satheesh Kumar, T Raghu, Pinaki P Bhattacharjee, G Appa Rao, and Utpal Borah. Strain rate dependent microstructural evolution during hot deformation of a hot isostatically processed nickel base superalloy. *Journal of Alloys and Compounds*, 681:28–42, 2016.
- [55] Y C Lin, Xian-Yang Wu, Xiao-Min Chen, Jian Chen, Dong-Xu Wen, Jin-Long Zhang, and Lei-Ting Li. EBSD study of a hot deformed nickel-based superalloy. *Journal of Alloys and Compounds*, 640:101–113, 2015.
- [56] Hongbin Zhang, Kaifeng Zhang, Haiping Zhou, Zhen Lu, Changhong Zhao, and Xiaoli Yang. Effect of strain rate on microstructure evolution of a nickel-based superalloy during hot deformation. *Materials & Design*, 80:51–62, 2015.
- [57] M Azarbarmas, M Aghaie-Khafri, J M Cabrera, and J Calvo. Dynamic recrystallization mechanisms and twinning evolution during hot deformation of Inconel 718. *Materials Science and Engineering: A*, 678:137–152, 2016.
- [58] Y L Hu, X Lin, Y L Li, S Y Zhang, X H Gao, F G Liu, X Li, and W D Huang. Plastic deformation behavior and dynamic recrystallization of Inconel 625 superalloy fabricated by directed energy deposition. *Materials & Design*, 186:108359, 2020.
- [59] Qingmiao Guo, Defu Li, Shengli Guo, Haijian Peng, and Jie Hu. The effect of deformation temperature on the microstructure evolution of Inconel 625 superalloy. *Journal of Nuclear Materials*, 414(3):440–450, 2011.
- [60] Qingmiao Guo, Defu Li, Haijian Peng, Shengli Guo, Jie Hu, and Peng Du. Nucleation mechanisms of dynamic recrystallization in Inconel 625 superalloy deformed with different strain rates. *Rare Metals*, 31(3):215–220, jun 2012.
- [61] Hongbin Zhang, Kaifeng Zhang, Shaosong Jiang, Haiping Zhou, Changhong Zhao, and Xiaoli Yang. Dynamic recrystallization behavior of a gamma prime-hardened nickel-based superalloy during hot deformation. *Journal of Alloys and Compounds*, 623:374–385, 2015.
- [62] Hongbin Zhang, Shengxue Qin, Huiping Li, Jie Liu, Yuting Lv, Yan Wang, Peng Zhang, Haiping Zhou, and Tao Wu. EBSD study of strain dependent microstructure evolution during hot deformation of a typical nickel-based superalloy. *Journal of Materials Research*, 34(2):321–334, 2019.

- [63] N D'Souza, W Li, C Argyrakis, G D West, and C D Slater. On the Evolution of Primary Gamma Prime Precipitates During High Temperature and High Strain Rate Deformation and Subsequent Heat Treatment in the Ni-Based Superalloy, RR1000. *Metallurgical and Materials Transactions A*, 50(9):4205–4222, 2019.
- [64] A NICOLAY, J M FRANCHET, J CORMIER, H MANSOUR, M DE GRAEF, A SERET, and N BOZZOLO. Discrimination of dynamically and post-dynamically recrystallized grains based on EBSD data: application to Inconel 718. *Journal of Microscopy*, 273(2):135–147, feb 2019.
- [65] Sukhdeep Singh, Fabian Hanning, and Joel Andersson. Influence of homogenisation treatments on the hot ductility of cast ATI® 718Plus®: Effect of niobium and minor elements on liquation characteristics. *Materials Science and Engineering: A*, 799:140151, 2021.
- [66] P Bereczki, B Fekete, V Szombathelyi, and F Misjak. Different Applications of the Gleeble® Thermal&ndash;Mechanical Simulator in Material Testing, Technology Optimization, and Process Modeling. *Materials Performance and Characterization*, 4(3):399–420, nov 2015.
- [67] George Ellwood Dieter. *Mechanical metallurgy*. McGraw-Hill series in materials science and engineering. McGraw-Hill, 3. ed. edition, 1986.
- [68] A Chamanfar, M Jahazi, J Gholipour, P Wanjara, and S Yue. Evolution of flow stress and microstructure during isothermal compression of Waspaloy. *Materials Science and Engineering: A*, 615:497–510, 2014.
- [69] A Amiri, M H Sadeghi, and G R Ebrahimi. Characterization of Hot Deformation Behavior of AMS 5708 Nickel-Based Superalloy Using Processing Map. *Journal of Materials Engineering and Performance*, 22(12):3940–3945, 2013.
- [70] R C Buckingham, C Argyrakis, M C Hardy, and S Biroasca. The effect of strain distribution on microstructural developments during forging in a newly developed nickel base superalloy. *Materials Science and Engineering: A*, 654:317–328, 2016.
- [71] Joseph I Goldstein, Dale E Newbury, Joseph R Michael, Nicholas W M Ritchie, John Henry J Scott, and David C Joy. *Scanning Electron Microscopy and X-Ray Microanalysis*. [electronic resource]. Springer New York, 4th ed. 20 edition, 2018.
- [72] Nicolas Brodusch, Hendrix Demers, and Raynald Gauvin. *Field Emission Scanning Electron Microscopy*. [electronic resource] : *New Perspectives for Materials Characterization*. SpringerBriefs in Applied Sciences and Technology. Springer Singapore, 1st ed. 20 edition, 2018.

- [73] F Bachmann, Ralf Hielscher, and Helmut Schaeben. Texture Analysis with MTEX – Free and Open Source Software Toolbox. *Solid State Phenomena*, 160:63–68, 2010.
- [74] Adam J Schwartz, Mukul Kumar, Brent L Adams, and David P Field. *Electron Backscatter Diffraction in Materials Science*. [electronic resource]. Springer US, 2nd ed. 20 edition, 2009.
- [75] Rahul Unnikrishnan, Shirley M Northover, Hedieh Jazaeri, and P John Bouchard. Investigating plastic deformation around a reheat-crack in a 316H austenitic stainless steel weldment by misorientation mapping. *Procedia Structural Integrity*, 2:3501–3507, 2016.
- [76] A Nicolaÿ, G Fiorucci, J.M. Franchet, J Cormier, and N Bozzolo. Influence of strain rate on subsolvus dynamic and post-dynamic recrystallization kinetics of Inconel 718. *Acta Materialia*, 174:406–417, aug 2019.
- [77] Adelajda Polkowska, Sebastian Lech, and Wojciech Polkowski. The effect of cold rolling degree on microstructure, crystallographic texture and mechanical properties of Haynes® 282® wrought nickel superalloy. *Materials Science and Engineering: A*, 787:139478, 2020.
- [78] Bingchao Xie, Baoyun Zhang, Hao Yu, Hao Yang, Qi Liu, and Yongquan Ning. Microstructure evolution and underlying mechanisms during the hot deformation of 718Plus superalloy. *Materials Science and Engineering: A*, 784:139334, 2020.
- [79] Meriem Zouari, Roland E Logé, and Nathalie Bozzolo. In Situ Characterization of Inconel 718 Post-Dynamic Recrystallization within a Scanning Electron Microscope, 2017.
- [80] Metzler D. and Fahrman M. G. The Effect of Prior TMP on Annealed Grain Size in HAYNES 282 Alloy, 2014.